Energy Reports 13 (2025) 117–139

Contents lists available at ScienceDirect

Energy Reports

journal homepage: www.elsevier.com/locate/egyr

Research paper

A rigorous optimization method for long-term multi-stage investment planning: Integration of hydrogen into a decentralized multi-energy system

Luka Bornemann *, Jelto Lange, Martin Kaltschmitt

Institute of Environmental Technology and Energy Economics, Hamburg University of Technology, Eissendorfer Strasse 40, 21073 Hamburg, Germany

ARTICLE INFO

Dataset link: https://doi.org/10.5281/zenodo.13902607

Keywords:
Green hydrogen
Multi-energy system
Multi-stage optimization
Rigorous optimization
Long-term planning
Mixed-integer linear programming

ABSTRACT

Thoroughly assessing future energy systems requires examining both their end states and the paths leading to them. Employing dynamic investment or multi-stage optimization models is crucial for this analysis. However, solving these optimization problems becomes increasingly challenging due to their long time horizons – often spanning several decades – and their dynamic nature. While simplifications like aggregations are often used to expedite solving procedures, they introduce higher uncertainty into the results and might lead to suboptimal solutions compared to non-simplified models. Against this background, this paper presents a rigorous optimization method tailored for multi-stage optimization problems in long-term energy system planning. By dividing the solution algorithm into a design and operational optimization step, the proposed method efficiently finds feasible solutions for the non-simplified optimization problem with simultaneous quality proof. Applied to a real-life energy system of a waste treatment plant in Germany, the method significantly outperforms a benchmark solver by reducing the computational time to find the first feasible solution from more than two weeks to less than one hour. Furthermore, it exhibits greater robustness compared to a conventional long-term optimization approach and yields solutions closer to the optimum. Overall, this method offers decision-makers computationally efficient and reliable information for planning investment decisions in energy systems.

1. Introduction

To limit the impact of climate change and comply with the Paris Climate Agreement (United Nations Framework Convention on Climate Change, 2015), the EU has made a legal commitment to achieve climate neutrality by 2050 (European Parliament and European Council, 2021). Some European countries, such as Germany (German Federal Government, 2021) and Sweden (Government Offices of Sweden - Ministry of the Environment and Energy, 2017), are already aiming for climate neutrality by 2045. To accomplish these targets within the remaining quarter of a century, environmentally and economically efficient solutions for the resulting demanding defossilization process are urgently needed.

In this regard, multi-energy systems promise a worthwhile option. By combining different energy carriers such as electricity, heat, as well as gases of fossil and renewable origin, cross-sectoral improvements (e.g., cost-effectiveness, reduction of greenhouse gas emissions, increased energy efficiency, improved reliability) can be achieved. Due to the complexity of multi-energy systems, employing optimization models becomes necessary to ascertain the approach for achieving these improvements (Brandon and Kurban, 2017; Ma et al., 2018; Mazzoni et al., 2019; Chertkov and Andersson, 2020). Within this context, the integration of green hydrogen has moved into the focus of science and industry in recent years (Welder et al., 2018; Stöckl et al., 2021; Fu et al., 2020; Navas-Anguita et al., 2020; Li et al., 2017) aiming, among others, to identify most promising hydrogen-based, or at least hydrogen-supported, energy systems. Typically, these models rely on static investment optimization, where a single target year represents the energy system's lifetime and only a single investment decision is made (Cuisinier et al., 2021).

However, when assessing potential transformation pathways of existing energy systems with the goal of achieving carbon neutrality by a specific year or following a designated reduction trajectory over time, static investment optimization approaches may not always be suitable. In this context, the examination of the type and timing of investment decisions is necessary (Pot et al., 2018), as these decisions influence the overall emitted emissions (Tong et al., 2019) and the total costs (Bütün et al., 2019; Pecenak et al., 2019) over the period under consideration. To allow for such investigations, dynamic investment optimization methods have to be applied. In this case, investments within multi-energy systems can be made over several stages; this

* Corresponding author.
E-mail address: luka.bornemann@tuhh.de (L. Bornemann).

https://doi.org/10.1016/j.egyr.2024.11.079
Received 6 August 2024; Received in revised form 8 October 2024; Accepted 27 November 2024
Available online 9 December 2024

Nomenclature

Latin letters

c	Price (EUR)
deg	Degradation (%)
$\dot{E}$	Energy demand (kW)
I	Component specific investment costs (EUR)
i	Discount rate (%)
M	Cost-curve fitting parameter (–)
n	Number of (–)
$\dot{Q}$	Power (kW)
Q	Capacity (kWh)
s	Investment stage (–)
SOC	State of charge (%)
t	Time step (h)
TC	Total costs (EUR)
w	Auxiliary variable (–)
$\boldsymbol{z}$	Surrogate vector of continuous variables (–)

Greek letters

α	Feasibility parameter (–)
Δ	Difference (–)
δ	Surrogate vector of binary variables (–)
ϵ	Optimality gap (–)
η	Efficiency (%)
μ	Long-term fitting parameter (–)

Sets

$\mathcal{C}$	Set of all components
$\mathcal{D}$	Set of all days
$\mathcal{E}$	Set of all energy carriers
$\mathcal{S}$	Set of all investment stages
$\mathcal{T}$	Set of all time steps
$\mathcal{TD}$	Set of all typical days

Superscripts

BAT	Battery
buy	Purchase
charge	Charging
CHP	Combined heat and power units
conv	Conversion component
Comp	Compressors
discharge	Discharging
ext	External
fix	Fixed
EL	Electrolyzer
el	Electricity
var	Variable
fee	Grid fees
final	Final
$\hat{}$	Aggregation
I	Investment costs
in	Input
inst	Installation
inter	Inter-period
intra	Intra-period
LB	Lower bound
life	Lifetime
max	Minimum
self	Self(discharging)
min	Maximum
main	Maintenance
nom	Nominal
old	Oldest
out	Output
PV	Photovoltaic
rel	Relative
ref	Reference
slack	Slack variable
sell	Sale
stor	Storage component
tax	Taxes
td	Typical day
$\tilde{}$	Fixed term
tot	Total
UB	Upper bound
y	Yearly

Subscripts

0	First element
c	Component
δ	Related to binary variables
d	Day
e	Energy carrier
el	Electricity
it	Iteration
s	Stage
seg	Segments
t	Time step
td	Typical day
z	Related to continuous variables

Abbreviations

B&C	Branch-and-Cut
BMR	Biomethanation reactor
CAPEX	Capital expenditures
CHP	Combined heat and power unit
EL	Electrolyzer
FC	Fuel cell
HP	Heat pump
HPC	High performance computing
MILP	Mixed integer linear programming
MES	Multi-energy system
NG	Natural gas
OPEX	Operational expenditures
PEM	Polymer electrolyte membrane
PV	Photovoltaic
TES	Thermal energy storage

type of optimization approach is therefore also referred to as multi-stage optimization (Cuisinier et al., 2021; Bakker et al., 2020). To clarify, the term 'multi-stage' in this paper refers to the investment planning characteristic of making decisions at predefined investment stages, as used by Mavromatidis and Petkov (2021). It is therefore not

to be confused with a multi-stage optimization algorithm, as shown, for example, in Baumgärtner et al. (2019a).

Since dynamic investment optimization methods incorporate long-term planning constraints, they require consideration of long time horizons (Deng and Lv, 2020). Simultaneously, a high temporal resolution is often necessary to adequately account for the fluctuations of supply-defined renewable energy sources. This results in large-scale optimization problems that demand substantial computational effort to solve (Kotzur et al., 2021), sometimes to the extent that no solutions can be found within acceptable time frames (Yokoyama et al., 2021).

To address these challenges, numerous decomposition methods have been developed in the literature to effectively reduce the computational burden of large-scale optimization problems without incurring additional uncertainties regarding optimality. In addition to general mathematical decomposition techniques such as Lagrangian decomposition (Sun et al., 2016) and Bender decomposition (Jacobson et al., 2023), there are methods that exploit the structural properties of energy system optimization problems (Yokoyama et al., 2002; Bahl et al., 2018; Baumgärtner et al., 2019a). Rather than solving the large-scale optimization problem directly, these methods efficiently solve specially tailored sub-optimization problems.

Nevertheless, these decomposition methods have primarily been adapted and applied in the context of static investment optimizations. In the realm of dynamic long-term investment optimization problems, mainly simplifications such as reducing the temporal and spatial resolution or simplifying the energy system model have been utilized thus far (Cuisinier et al., 2021). For example, Vakilifard et al. (2019) developed a two-level mixed-integer linear programming (MILP) optimization approach investigating a multi-period long-term planning model of an urban water and energy supply system using different time resolutions. Pecenak et al. (2019) applied an adaptive multi-year optimization method on a Southern California microgrid and reduce computational time by using a myopic approach combined with a temporal resolution of typical days. Nevertheless, while the myopic approach may better reflect real investment decision-making, it does not guarantee that the optimum of the entire time horizon will be obtained (Cuisinier et al., 2021). Mavromatidis and Petkov (2021) developed a multi-stage energy optimization framework that supports perfect foresight, multiple spatially distributed multi-energy systems, and modeling of each energy system component as a distinct unit. The authors applied their framework to a case study of an energy system of a hypothetical district in Zurich, Switzerland. They consider a period of 30 years until 2050, where the yearly resolution consists of a set of typical days. The use of typical periods brings disadvantages (e.g., loss of chronology, unclear number of necessary periods, robustness of multi-energy system sizing Kotzur et al., 2021), which can lead to suboptimal or even infeasible solutions. Prina et al. (2019) present a long-term energy planning method with perfect foresight coupling a Multi-Objective Evolutionary Algorithm and the energy system simulation tool EnergyPLAN. The authors overcame the weaknesses of aggregated time periods by using an hourly resolution. However, the genetic algorithm used is not a deterministic optimization method (i.e., finding an optimal solution is not guaranteed).

As evident, there are various approaches to address the computational challenges of dynamic long-term investment optimization. However, due to simplifications (e.g., temporal aggregation, heuristic, and myopic optimization methods), most of these approaches lack the guarantee of finding the optimal transformation path. To achieve this, deterministic or rigorous optimization methods are necessary.

Against this background, the goal of this paper is the development of a rigorous method for dynamic long-term investment optimization related to cost minimization. The presented method provides a solution as well as a quality proof for the non-simplified optimization problem within a reasonable time period. Moreover, the method guarantees that a desired optimality gap of the non-simplified optimization problem is reached in finite time. It combines state-of-the-art MILP static investment modeling techniques (e.g., distinct unit models, part-load performance, investment costs curves) with multi-stage optimization techniques (e.g., perfect foresight, technical and economic developments, lifetime, degradation) while considering an economic objective function.

To demonstrate the functionality of the presented method, the proposed method is applied to a real-life example of a multi-energy system of a waste treatment company in Germany. Based on various scenarios, optimal transformation pathways from an economic point of view are identified. This case study allows for the demonstration of the method's performance and the economic feasibility of integrating hydrogen production and usage into a decentralized multi-energy system.

The remainder of the paper is structured as follows. Section 2 presents the mathematical formulation of the dynamic investment optimization problem and the rigorous optimization method. In Section 3, the investigated case study including the considered scenarios is defined. Following, the proposed method is applied to the case study, and the results are presented and discussed. Finally, the conclusions are given in Section 4.

2. Methodology

The methodology of this paper is outlined here. Initially, a generic dynamic investment optimization problem is defined, providing the foundation for the subsequent rigorous optimization method. Following this, the rigorous optimization method employed to solve this dynamic investment optimization problem is described in detail. The methodology is intentionally described in a general manner, ensuring its universal applicability to a wide range of case studies.

2.1. Model formulation

Below, the unique characteristics of dynamic investment planning optimization as well as the mathematical model formulation are discussed. Dynamic investment planning involves the fact that certain investment decisions can be made at specific points in time. Such a decision can be, for example, the replacement of components that reached their end of life or the addition of new components due to an increasing energy demand or other newly over time emerging constraints. To clarify, the end of life can be justified both technically and economically. In this paper, no distinction is made between the two and only the end of life is referred to.

In the context of this work, therefore, the considered time horizon is divided into so-called 'investment stages' ($s \in S$) (Mavromatidis and Petkov, 2021). The sequence of these investment stages imparts a multi-stage character to the underlying optimization problem. Therefore, dynamic investment planning optimization is referred to below as multi-stage optimization. At the beginning of each investment stage, the assessed energy system configuration may change in a way that selected system components reaching their end of life are removed, and new ones might be added. Within an investment stage (i.e., until the beginning of the following investment stage), the configuration of the energy system remains unchanged. In addition, selected components existing within the respective energy system may degrade throughout an investment stage; i.e., at the beginning of the subsequent investment stage either their installed capacity (storage components) or their efficiency (conversion components) decreases.

Each investment stage consists of a selected number of years n_s^y. The lower the number of years per investment stage or, in other words, the higher the number of investment stages, the more precisely the calculated solution will reflect the optimal real transformation pathway. However, this also leads to an increase in computational effort. Therefore, it is essential to find a satisfactory compromise between accuracy and computing time.

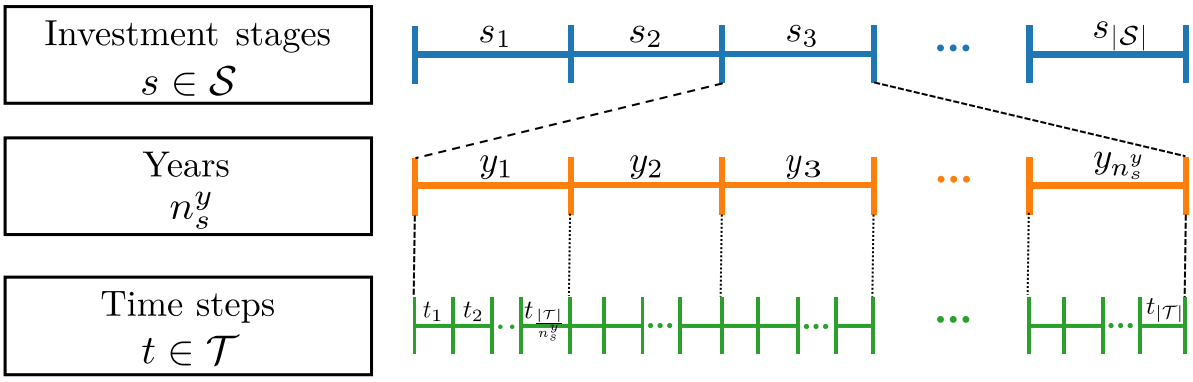

Fig. 1. Time horizon and temporal indices used in this work.
Source: Adapted from Mavromatidis and Petkov (2021).

Additionally, each year, delineated as the smallest time period within an investment stage, is subdivided into a predetermined number of hourly time steps. This ensures uniformity across all investment stages, with each investment stage comprising an equivalent number of time steps ($t \in \mathcal{T}$). A graphical overview of the time horizon defined here is given in Fig. 1.

2.1.1. Multi-stage optimization problem

The mathematical formulation of the multi-stage optimization problem is presented below. In the following, the main text highlights equations essential for understanding multi-stage optimization. Additional equations (e.g., unit models, cost calculations) are provided in the Appendix for reference. Generally, within multi-stage optimization, the multi-energy system under examination can be optimized with respect to technical, economic, and/or environmental objectives.

However, for the scope of this paper, the focus is solely put on economic optimization. Accordingly, the multi-stage optimization aims to minimize all costs incurred over the entire time horizon (i.e., perfect foresight is assumed). Thus, the objective function minimizes the total costs TC (Eq. (1)). To minimize total costs, the design of the multi-energy system is optimized in terms of installed capacities $Q_{c,s}$ ($\forall s \in S$) and the operation in terms of the input and output power $\dot{Q}_{c,s,t,e}$ of each component ($\forall t \in \mathcal{T}$). Therefore, the sets $\mathcal{C}$ and $\mathcal{E}$ are defined including each energy system component ($\forall c \in C$) and energy carrier ($\forall e \in \mathcal{E}$), respectively. Furthermore, the subset $\mathcal{E}^{ext}$ $\left(\mathcal{E}^{ext} \subset \mathcal{E}\right)$ includes those energy sources that can either be bought or sold externally. The total costs TC are calculated by the sum of the investment costs $CAPEX_s$, fixed operating costs $OPEX_s^{fix}$ and variable operating costs $OPEX_s^{var}$ over all investment stages ($\forall s \in S$).

The investment costs $CAPEX_s$ of each investment stage ($\forall s \in S$) are derived from the investment costs $I_{c,s}$ of each component ($\forall c \in C$), multiplied by an annuity factor (based on the lifetime n_c^{life} of component c and the discount rate i) and the number of years per investment stage n_s^y. The investment costs $I_{c,s}$ are calculated according to Eqs. (A.12) and (A.13). Thus, the absolute investment costs are not used. Correspondingly, the investment costs of each component $I_{c,s}$ are annualized for the period in which they exist (i.e., capital-linked costs). If a component is removed from the respective multi-energy system due to reaching its end of life in investment stage s, its annualized investment cost contribution becomes zero. This approach avoids favoring inexpensive technologies to purchase over technologies with inexpensive operating costs at the end of the time period.

The fixed operating costs $OPEX_s^{fix}$ are derived from the product of the investment costs $I_{c,s}$ and a maintenance factor c_c^{main}, while the variable costs $OPEX_s^{var}$ are based on the difference between the costs for the external purchase $c_{s,t,e}^{buy}\dot{Q}_{s,t,e}^{buy}$ and the income from the sale $c_{s,t,e}^{sell}\dot{Q}_{s,t,e}^{sell}$ of energy carriers $\left(\forall e \in \mathcal{E}^{ext} \subset \mathcal{E}\right)$.

$$\min_{Q_{c,s},\dot{Q}_{c,s,t,e}^{out},\dot{Q}_{c,s,t,e}^{in},\dot{Q}_{s,t,e}^{buy},\dot{Q}_{s,t,e}^{sell},\boldsymbol{z},\boldsymbol{\delta}} \quad TC$$

$$\text{with} \quad TC = \sum_{s \in S} CAPEX_s + OPEX_s^{fix} + OPEX_s^{var}$$

$$CAPEX_s = n_s^y \sum_{c \in C} I_{c,s} \frac{i(1+i)^{n_c^{life}}}{(1+i)^{n_c^{life}} - 1} \tag{1}$$

$$OPEX_s^{fix} = n_s^y \sum_{c \in C} I_{c,s} c_c^{main}$$

$$OPEX_s^{var} = \sum_{t \in \mathcal{T}} \sum_{e \in \mathcal{E}^{ext}} \Delta t_t \left(c_{s,t,e}^{buy}\dot{Q}_{s,t,e}^{buy} - c_{s,t,e}^{sell}\dot{Q}_{s,t,e}^{sell} \right)$$

The multi-stage optimization problem is further constrained via Eqs. (2a)–(2c), following the formulation employed by Wang et al. (2024). Eq. (2a) represents the energy balances regarding exogenous energy demands $\dot{E}_{s,t,e}$ which have to be fulfilled for every energy carrier ($\forall e \in \mathcal{E}$) in every time step ($\forall t \in \mathcal{T}$). All further constraints (e.g., part-load performance, on/off decisions, storage balances, cost curves) are expressed via Eq. (2b). Following on from this, all optimization variables are listed in Eq. (2c), with vectors $\boldsymbol{z}$ and $\boldsymbol{\delta}$ summarizing all other decision variables (e.g., part-load performance, on/off decisions, cost curves) not further specified here. Further specifications of constraints and variables can be found in Appendices A.1.1 and A.1.2.

$$\sum_{c \in C} \left(\dot{Q}_{c,s,t,e}^{\text{out}} - \dot{Q}_{c,s,t,e}^{\text{in}} \right) + \left(\dot{Q}_{s,t,e}^{\text{buy}} - \dot{Q}_{s,t,e}^{\text{sell}} \right) = \dot{E}_{s,t,e}, \quad \forall s \in S, \forall t \in \mathcal{T}, \forall e \in \mathcal{E} \tag{2a}$$

$$\boldsymbol{g}(Q_{c,s}, \dot{Q}_{c,s,t,e}^{out}, \dot{Q}_{c,s,t,e}^{in}, \dot{Q}_{s,t,e}^{buy}, \dot{Q}_{s,t,e}^{sell}, \boldsymbol{z}, \boldsymbol{\delta}) \leq \boldsymbol{0}, \tag{2b}$$

$$Q_{c,s}, \dot{Q}_{c,s,t,e}^{out}, \dot{Q}_{c,s,t,e}^{in}, \dot{Q}_{s,t,e}^{buy}, \dot{Q}_{s,t,e}^{sell} \in \mathbb{R}^+, \boldsymbol{z} \in \mathbb{R}^{n_z}, \boldsymbol{\delta} \in \{0,1\}^{n_\delta} \tag{2c}$$
$$\forall s \in S, \forall c \in C, \forall t \in \mathcal{T}, \forall e \in \mathcal{E}$$

2.1.2. Multi-stage constraints

Each energy system component is considered as a distinct unit characterized by a possible component-specific degradation and a fixed end of life. The progress of the degradation $deg_{c,s}$ is derived from the component-specific yearly degradation rate deg_c^y, the investment stage s^{inst}, in which the specific component is installed, and the number of years per investment stage n_s^y (Eq. (3)).

$$deg_{c,s} = \left(1 - deg_c^y\right)^{(s - s^{inst}) n_s^y} \tag{3}$$

Further, a differentiation between energy conversion components ($c \in C^{conv} \subset C$) and energy storage components $\left(c \in C^{stor} = C \setminus C^{conv}\right)$, and their respective degradation mechanism is made. A decrease in efficiency $\eta_{c,s}^{nom}$ is assumed to be the dominant degradation mechanism for energy conversion components, while a decrease in capacity $Q_{c,s}$ is assumed to be the dominant degradation mechanism for energy storage

components. Accordingly, assuming degradation, the capacity of energy storage components (e.g., battery) decreases during their lifetime. In contrast, the capacity of energy conversion components (e.g., heat pump) built in investment stage s^{inst} remains constant until their end of life (Eq. (4)). The capacity of both component types becomes zero, reaching the end of life. Consequently, the respective component is removed from the investigated energy system and, thus, drops out of the accounting of annualized investment costs $CAPEX_s$ (Eq. (1)).

$$Q_{c,s} = \begin{cases} Q_{c,s^{inst}}, & \text{for } s^{inst} \le s \le s^{inst} + \frac{n_c^{life}}{n_s^y}, \quad \forall c \in C^{conv} \\ Q_{c,s^{inst}}\, deg_{c,s}, & \text{for } s^{inst} \le s \le s^{inst} + \frac{n_c^{life}}{n_s^y}, \quad \forall c \in C^{stor} \\ 0, & \text{for } s > s^{inst} + \frac{n_c^{life}}{n_s^y}, \quad \forall c \in C \end{cases} \tag{4}$$

Following on from this, degradation influences the nominal efficiency $\eta_{c,s}^{nom}$ of the respective energy conversion components (e.g., battery) (Eq. (5)). In contrast to their capacity, their nominal efficiency decreases with increasing age. The charging and discharging efficiencies $\eta_{c,s}^{(dis)charge}$ of the energy storage components are not affected by degradation.

$$\begin{aligned} \eta_{c,s}^{nom} &= \eta_{c,s^{inst}}^{nom}\, deg_{c,s}, && \forall c \in C^{conv} \\ \eta_{c,s}^{(dis)charge} &= \eta_{c,s^{inst}}^{(dis)charge}, && \forall c \in C^{stor} \end{aligned} \tag{5}$$

2.2. Rigorous optimization method

The rigorous optimization method for solving the previously introduced multi-stage optimization problem is presented here. For this purpose, the terminology is clarified first.

- The 'original problem' is defined as the multi-stage optimization problem with full time series (i.e., no temporal aggregation) and distinct unit modeling (i.e., no technical aggregation).
- A 'feasible solution', which serves as an upper bound, is defined as a solution to this original problem.
- A 'rigorous method' ensures certainty in reaching a global minimum within specified tolerances (Neumaier, 2004).

Since solving the original problem is computationally intractable, a rigorous optimization method, introduced by Baumgärtner et al. (2019a,b), is employed to attain a feasible solution with manageable computational effort and to assess its quality. The rigorous optimization method generally consists of two parts, dividing the method into an upper and lower bound branch.

- Within the upper bound branch, a feasible solution to the original problem is obtained.
- In the lower bound branch, a lower bound is obtained, which serves as a quality proof of the feasible solution gained in the upper bound branch.

The method iteratively improves the obtained upper bounds and lower bounds until a desired solution quality is provided, thereby endowing the optimization methodology with deterministic or rigorous properties (Neumaier, 2004). To adapt this method for solving a multi-stage optimization problem, certain methodological aspects need to be modified or extended. These necessary adaptations and their resulting method are presented in the following sections. Fig. 2 provides a graphical overview. For further background information regarding the original method, the reader is referred to Baumgärtner et al. (2019a,b).

2.2.1. Upper bound

In the upper bound branch, the problem size is initially reduced by two aggregation steps. Subsequently, a design optimization (i.e., simultaneous optimization of the design and operation of the multi-energy system) is conducted based on this aggregated problem. The outcome of this design optimization is a so-called 'design candidate' (Baumgärtner et al., 2019b), outlining the structure of the investigated multi-energy system at each investment stage. Following this, a year-wise operational optimization based on the full time series is carried out for the design candidate, aiming to identify infeasible time steps and calculate a feasible solution. Consequently, an upper bound is determined. These various steps are outlined below.

Step 1: Aggregation. Initially, the problem size is reduced by two aggregation steps discussed below.

Time series aggregation First, the temporal resolution is simplified using time series aggregation, where the full time series is clustered into a predetermined number of typical days n_{td}. Within each typical day, adjacent time steps are, in turn, clustered into a selected number of segments n_{seg} to further reduce the temporal resolution. The combined length of all segments totals 24 h. To accurately represent long-term storage cycles, the storage formulation from Kotzur et al. (2018) is used. More detailed information can be found in Appendix A.1.1 in Eqs. (A.8)–(A.11).

Component aggregation Secondly, the technical resolution is reduced by employing a component-wise aggregation. Instead of modeling the energy system components as distinct units with nominal capacity $Q_{c,s}$, all components of one type are combined into one aggregated component with the overall nominal capacity $\hat{Q}_{c,s}$ $\left(\forall c \in \hat{C} \subset C\right)$. The addition of new components or the removal of old components of the same type is then represented by a respective change in nominal capacity $\Delta\hat{Q}_{c,s}$. Despite the summation of nominal capacity within the aggregated component, it is crucial for the aggregated component's operation to reflect that of the distinct units within it (e.g., different on/off or load states). Therefore, the permissible load range of the distinct unit cannot be directly transferred to the aggregated component. Thus, in this step, the corresponding constraints (Eq. (A.2)) are deactivated, allowing the full load range to be available for the aggregated component.

Furthermore, component-wise aggregation leads to a combination of different efficiencies (e.g., due to degradation or improved efficiencies of newly built units) within one aggregated component. For this reason, the average aggregated nominal efficiency $\hat{\eta}_{c,s}^{nom}$ is introduced for each aggregated component $\left(\forall c \in \hat{C}\right)$. The average aggregated nominal efficiency is calculated as the capacity weighted average value of all components of the same type built during the investment period $\left(\hat{s} \in \left[s^{old}, s\right]\right)$, initiating from the investment stage of the oldest component still in operation s^{old} and extending to the current investment stage s (Eq. (6)).

$$\hat{\eta}_{c,s}^{nom} = \frac{\sum_{\hat{s}\in[s^{old},s]} \eta_{c,\hat{s}}^{nom}\, deg_{c,\hat{s}}\, \Delta\hat{Q}_{c,\hat{s}}}{\sum_{\hat{s}\in[s^{old},s]} \Delta\hat{Q}_{c,\hat{s}}} \quad \forall s \in S, \forall c \in \hat{C} \tag{6}$$

$$\text{with} \quad s^{old} = \max(s_1, s - \frac{n_c^{life}}{n_s^y})$$

To integrate the nonlinear equation into the MILP optimization problem, Eq. (6) is approximated by a linear relationship in Eq. (7). Thus, the average aggregated nominal efficiency $\hat{\eta}_{c,s}^{nom}$ is the arithmetic mean of the degraded efficiency of the oldest components under operation (built in s^{old}) and the efficiency of newly built components in the current investment stage s (Eq. (7)).

$$\hat{\eta}_{c,s}^{nom} = 0.5\left(\eta_{c,s}^{nom} + \eta_{c,s^{old}}^{nom}\, deg_{c,s}\right) \quad \forall s \in S, \forall c \in \hat{C} \tag{7}$$

Step 2: Aggregated design optimization. With the problem size significantly reduced by time series aggregation $\left(n_{td} \times n_{seg} \ll |\mathcal{T}|\right)$ and component-wise aggregation $\left(|\hat{C}| < |C|\right)$, the resulting problem (Eqs. (1) and (2a)–(2c)) can be effectively solved. This yields a so-called 'design candidate' (Baumgärtner et al., 2019b) of the assessed multi-energy system, determining which component is to be added to the multi-energy system at a given time with a designated capacity. It, thus, defines the structure of the multi-energy system for each investment stage $(\forall s \in S)$. The aggregated design optimization step corresponds to a widely used approach for solving multi-stage optimization problems (Bohlayer et al., 2021; Pecenak et al., 2019; Mavromatidis and Petkov, 2021; Cuisinier et al., 2021).

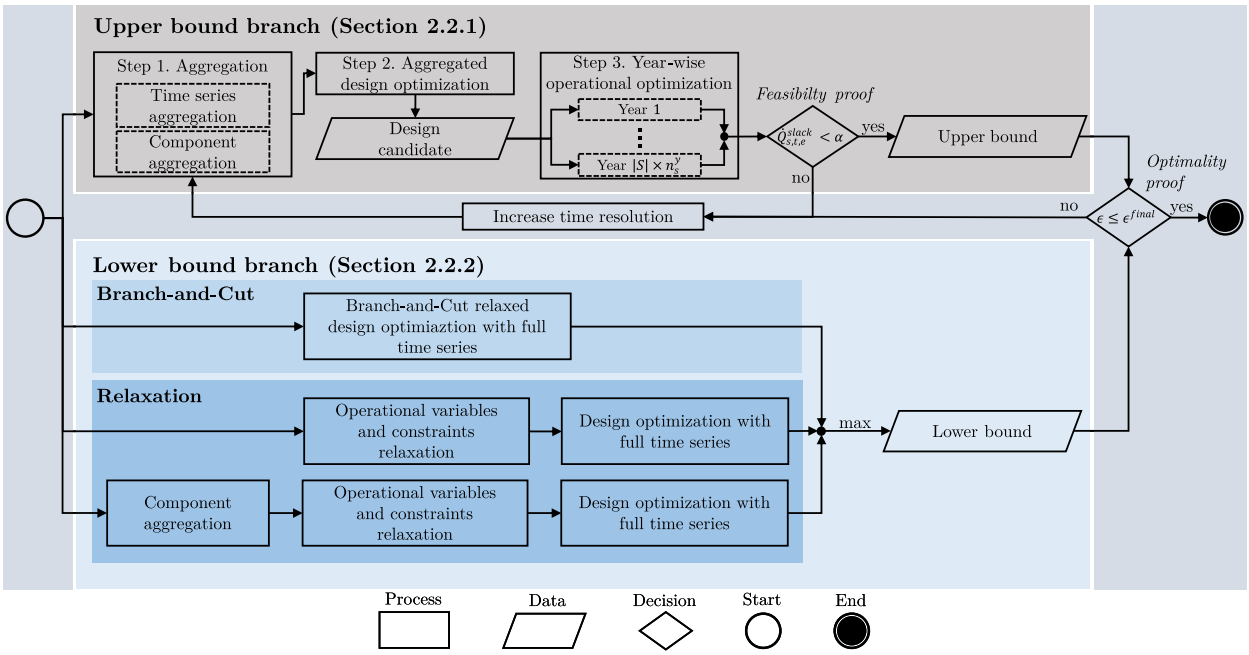

Fig. 2. Overview of the rigorous optimization method to solve multi-stage optimization problems.
Source: Adapted from Baumgärtner et al. (2019a,b).

Step 3: Year-wise operational optimization. The aggregation steps undertaken obscure the precise operational details of this design candidate. Consequently, to ascertain its feasibility, an operational optimization is conducted based on this design candidate as part of the search for a feasible solution. By optimizing the operation separately, it can be determined if the design candidate can fulfill the energy demands at each time step ($\forall t \in \mathcal{T}$) of the full time series (feasible solution) and evaluate the corresponding operational costs (upper bound). For this purpose, the full time series is applied to the design candidate for each year independently. Consequently, $|S| \times n_s^y$ operational optimization problems are solved subsequently.

Before the operational optimization, the component-wise aggregation from Step 1 is reverted. For this purpose, for each aggregated component $\left(\forall c \in \hat{C}\right)$, the change in nominal capacity $\Delta\hat{Q}_{c,s}$ is converted into the addition of a distinct energy system component with equivalent nominal power $Q_{c,s}$ $(c \in C)$. Since this allows to look at the operational behavior of each distinct component, partial-load constraints are reactivated (Eq. (A.2)). In Step 2, all technical properties and operational characteristics of a component type were previously consolidated into a single unit. However, now the expansion of capacity is addressed by introducing a new unit of the corresponding component type, each with its own distinct properties and independent operating behavior.

To detect infeasible time steps (e.g., time steps in which the energy demands cannot be fulfilled), slack variables $\dot{Q}_{s,t,e}^{slack}$ are introduced for each energy carrier ($\forall e \in \mathcal{E}$) as proposed by Teichgraeber et al. (2020). In this context, each slack variable represents an unlimited and readily available source of the energy carrier e, intended to be accessed only when the corresponding energy demand cannot be met by other means. To achieve this, these slack variables are added to the objective function and assigned a slack price c^{slack}. The latter should be chosen to be a multiple larger than the remaining energy prices $c_{s,t,e}^{buy}$ and $c_{s,t,e}^{sell}$, respectively. Consequently, utilizing these slack variables is deemed economically unviable. If, however, a slack variable is used in a time step t $\left(\dot{Q}_{s,t,e}^{slack} > \alpha\right)$, this indicates an infeasible time step. A time step t is considered feasible for values smaller than α in order to minimize the influence of numerical inaccuracies.

Therefore, within Step 3, the operational optimization problem for each investment stage ($\forall s \in S$) is solved year-wise ($t \in \mathcal{T}^y \subset \mathcal{T}$) (Eq. (8)). As the design candidate from the aggregated optimization is used, all design variables $Q_{c,s}$, along the investment costs $CA\tilde{P}EX_s$ and fixed operating costs $OP\tilde{E}X_s^{fix}$, are fixed. A tilde sign connotes fixed terms. Additionally, energy balance constraints (Eq. (2a)) are relaxed by adding slack variables $\dot{Q}_{s,t,e}^{slack}$ in Eq. (8b).

$$\min_{\dot{\boldsymbol{Q}},\boldsymbol{z},\boldsymbol{\delta}} \quad CA\tilde{P}EX_s + OP\tilde{E}X_s^{fix} + OPEX_s^{var} + \sum_{t\in\mathcal{T}} c^{slack}\dot{Q}_{s,t,e}^{slack}, \tag{8a}$$

$$\forall s \in S, \forall t \in \mathcal{T}^y \subset \mathcal{T}$$

$$\text{s.t.} \sum_{c\in C}\left(\dot{Q}_{c,s,t,e}^{\text{out}} - \dot{Q}_{c,s,t,e}^{\text{in}}\right) + \left(\dot{Q}_{s,t,e}^{\text{buy}} - \dot{Q}_{s,t,e}^{\text{sell}}\right) + \dot{Q}_{s,t,e}^{slack} = \dot{E}_{s,t,e}, \tag{8b}$$

$$\forall t \in \mathcal{T}^y \subset \mathcal{T}, \forall e \in \mathcal{E}$$

$$\boldsymbol{g}(\dot{\boldsymbol{Q}}, \boldsymbol{z}, \boldsymbol{\delta}) \leq \boldsymbol{0} \tag{8c}$$

$$\text{with} \quad \dot{\boldsymbol{Q}} = \left\{\dot{Q}_{c,s,t,e}^{out}, \dot{Q}_{c,s,t,e}^{in}, \dot{Q}_{s,t,e}^{buy}, \dot{Q}_{s,t,e}^{sell}, \dot{Q}_{s,t,e}^{slack}\right\}$$

Feasibility proof and upper bound. Finally, if the full time series proves to be feasible (i.e., all slack variables are smaller than α), the solution of each operational optimization problem is summed up and, thus, a feasible solution and an upper bound TC^{UB} of the original problem is obtained. Alternatively, if any slack variable surpasses the threshold α, the segment (e.g., a day) of the full time series with the highest slack variable value is isolated and integrated into the aggregated time series in the subsequent iteration. The upper bound is continuously improved by augmenting the number of typical days considered in each subsequent iteration within Step 1, thereby increasing the time resolution.

2.2.2. Lower bound and optimality gap

To calculate a lower bound TC^{LB}, a Relaxation and a Branch-and-Cut branch are applied in parallel.

Relaxation. In the relaxation branch, a lower bound is calculated in two ways. First, the original problem (Eqs. (1) to (5)) is relaxed without aggregation (Pure Relaxation). In the second approach, the original problem is both relaxed and component-wise aggregated (Aggregation & Relaxation). Due to both relaxations, its optimum represents a lower bound of the original problem. This subdivision is performed because

both paths exhibit different degrees of relaxation of the original problem, resulting in variations in the tightness of the lower bound and the computing time required. The Aggregation & Relaxation (AR) branch is expected to quickly calculate a comparatively weaker lower bound, while the Pure Relaxation (PR) branch requires more time to compute a tighter lower bound. Early knowledge of a lower bound is necessary to quantify the initial solutions of the upper bound branch.

Pure relaxation Within the Pure Relaxation (PR) branch, all operational binary variables are removed from the original problem (Eqs. (1) to (5)), and the associated constraints are relaxed. This eliminates the restriction of the load range (Eqs. (A.2) and (A.3)), allowing the full load range to be utilized (Eq. (9)).

$$0 \leq \dot{Q}^{out}_{c,s,t,e} \leq \dot{Q}^{rel,UB}_{c} Q_{c,s}, \quad \forall s \in \mathcal{S}, \forall t \in \mathcal{T}, \forall c \in \mathcal{C} \tag{9}$$

In addition, simultaneous charging and discharging of the storage components is permitted, so that Eq. (A.6) is replaced by Eq. (10).

$$\begin{aligned} \dot{Q}^{out}_{c,s,t,e} &\leq \dot{Q}^{rel,UB}_{c} Q_{c,s} \\ \dot{Q}^{in}_{c,s,t,e} &\leq \dot{Q}^{rel,UB}_{c} Q_{c,s} \\ \forall s \in \mathcal{S}, \forall t \in \mathcal{T}, \forall c \in \mathcal{C}^{stor} & \end{aligned} \tag{10}$$

The PR optimization problem is solved afterwards.

Aggregation & relaxation In the Aggregation & Relaxation (AR) Branch, the original problem (Eqs. (1) to (5)) is first aggregated component-wise (see Section 2.2.1, Step 1). To ensure a true relaxation, the calculation of the average aggregated nominal efficiency $\hat{\eta}^{nom}_{c,s}$ (Eq. (7)) is adjusted so that the nominal efficiency applies to the aggregated component for each stage (Eq. (11)).

$$\hat{\eta}^{nom}_{c,s} = \eta^{nom}_{c,s} \quad \forall s \in \mathcal{S}, \forall c \in \hat{\mathcal{C}} \tag{11}$$

The relaxation method from the Pure Relaxation (PR) branch is then applied, and the resulting relaxed optimization problem is solved.

Branch-and-cut. Since the relaxation branch described above are limited in their final lower bounds, the Branch-and-Cut (B&C) branch (Baumgärtner et al., 2019b) is executed in parallel for the identification of an updated lower bound TC^{LB}. Here, the original problem with full time series is solved via state-of-the-art MILP solver. Although solving the original problem in its entirety is computationally challenging within a reasonable time frame, the B&C branch is adept at regularly providing updated lower bounds.

Optimality gap. Finally, the tightest and hence the maximum lower bound is selected from the lower bounds calculated across the branches. This lower bound serves the purpose of validating the quality of the solutions obtained in Section 2.2.1 by calculating an optimality gap ϵ via Eq. (12). The rigorous optimization method concludes upon reaching the desired optimality gap ϵ^{final} or a user-defined time limit t^{final} at the end of the latest iteration t_{it} Eq. (13).

$$\epsilon = \frac{TC^{UB} - TC^{LB}}{TC^{UB}} \leq \epsilon^{final} \tag{12}$$

$$t_{it} \geq t^{final} \tag{13}$$

3. Case study: Waste treatment plant

To demonstrate the functionality of the universal method presented and the insights it can offer, the method is applied to a specific case study. This case study involves a detailed examination of the multi-stage integration of hydrogen into a decentralized multi-energy system. Presented below is the superstructure of the assessed multi-energy system, along with details concerning the input data and the defined scenarios. Following this, the results obtained are presented and discussed. Due to its inherent general applicability, this method could also be applied to various other case studies.

3.1. Case study definition

The case study is based on a real-life multi-energy system of a waste treatment plant located in Lübeck, Germany (Entsorgungsbetriebe Lübeck, 2020). A 25-year transformation period (the year 2022 till the year 2047) is examined. Based on an initial system configuration, the aim of the optimization is to develop this multi-energy system at minimal cost, ensuring the fulfillment of all energy demands throughout the entire assessment period. The types of energy demand remain unchanged, but potential variations in the magnitude of the energy demands over the years are taken into consideration. A total of 6 scenarios are derived from these potential developments. These scenarios aim to showcase the robustness of the presented rigorous optimization method by varying the solution space for the transformation path of this multi-energy system and the feasible set of the underlying optimization problem.

3.1.1. Multi-energy system definition

Superstructure. As an integral aspect of a research project (Entsorgungsbetriebe Lübeck, 2022) and as the primary focus of the study, the investigated multi-energy system (Fig. 3) must cover a defined hydrogen demand at 250 bar. To meet this hydrogen demand, a hydrogen production process chain consisting of a polymer electrolyte membrane electrolyzer (PEMEL), a hydrogen compressor, and a compressed hydrogen storage at 250 bar is considered. Additionally, the produced hydrogen can be used energetically within a polymer electrolyte membrane fuel cell (PEMFC) and act as a feedstock for a subsequent methanation of the CO_2 contained within biogas, leading to the production of biomethane. The biomethane can be fed into the natural gas grid to generate revenues.

Furthermore, the defined multi-energy system has to cover an electricity and heat demand. For this purpose, various components are considered, including biogas-driven heat and power units (CHP), heat pumps (HP), and photovoltaic (PV) systems. To enhance the flexibility of electricity and heat provision, thermal energy storages (TES), batteries, and biogas storage units are incorporated. Given that the heat demand primarily arises from preheating processes within the waste treatment plant, where a feed temperature of 60 °C suffices, the waste heat integration of the polymer exchange membrane electrolyzer, fuel cell, and methanation processes is explored.

Moreover, the multi-energy system is connected to the public electricity grid allowing for the purchase of electricity as well as the sale of electricity surpluses. Additionally, there is a link to the on-site biogas grid, enabling the consumption of biogas.

The modeling of the energy system components relies on input–output relationships outlined in Eqs. (A.1) to (A.11).

Design task. In its current state, the investigated multi-energy system comprises a biogas storage facility and two biogas-driven heat and power units. This is regarded as the starting point, representing the initial state as of the base year 2022. Based on this initial state, the aim of the optimization is to further develop the multi-energy system at minimal cost, ensuring the fulfillment of all energy demands throughout the entire examination period. All other components listed above are potential additions for expanding the multi-energy system, commencing with the first investment stage in the year 2022.

3.1.2. Input data

The input time series parameters for this analysis encompass the outlined energy demands and energy prices. Each parameter is associated with an annual reference profile in hourly resolution, depicting the current and, consequently, the initial situation. Additionally, development paths with low and high values are assigned to each input parameter to illustrate potential future developments. These development pathways encapsulate the total annual energy demand and the average annual energy price for each energy demand and energy price, respectively. Leveraging the assigned values, the hourly profiles are appropriately scaled for the corresponding year.

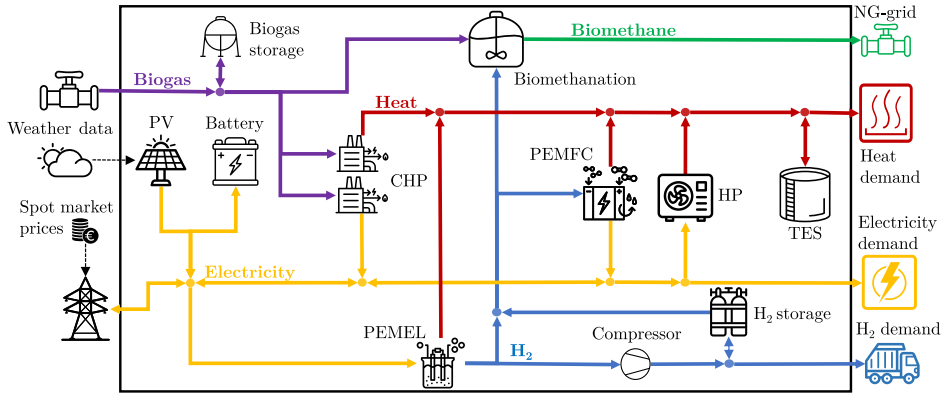

Fig. 3. Superstructure of the considered multi-energy system. (PV: Photovoltaics, CHP: Biogas-driven combined heat and power unit, PEMFC: Polymer electrolyte membrane fuel cell, PEMEL: Polymer electrolyte membrane electrolyzer, HP: Heat pump, TES: Thermal energy storage, NG: Natural gas).

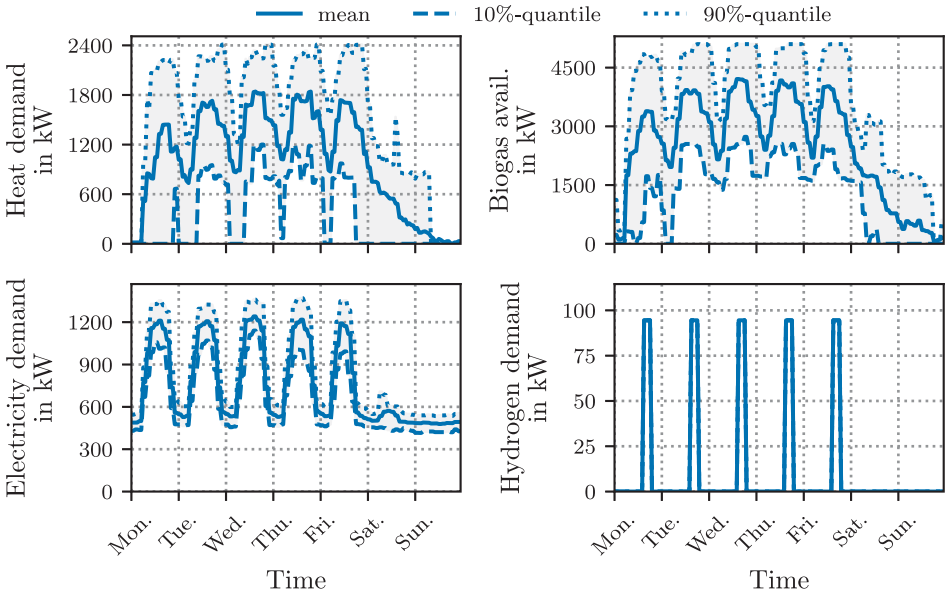

Fig. 4. Hourly reference profile of the energy demands. The demand profile is represented by week-wise mean, 10 %- and 90 %-quantiles.

Initial state. To begin, the input time series parameters are presented, reflecting the initial conditions starting with the first investment stage in the year 2022. The reference profiles of each energy demand assumed here are shown in Fig. 4. The reference profiles for the electricity and heat demand as well as the available biogas are derived from measurements. The hydrogen demand is based on a daily refueling profile, with refueling occurring on weekday afternoons outside the main work shift and excluding weekends. The weekday amount of hydrogen is based on a complete tank filling of a reference vehicle with a 12 kg hydrogen tank (ZÖLLER-KIPPER GmbH, 2022) within 4 h. Only the amounts of energy to be supplied are taken into consideration; the actual refueling is not considered and is outside the system boundary. Consequently, it is assumed that within the considered energy system, hydrogen is supplied and compressed to a pressure level of 250 bar, which is the typical storage pressure for hydrogen tanks (Barthelemy et al., 2017). The final compression and cooling required for refueling occur at the filling station, which lies beyond the defined system boundary.

Furthermore, hourly electricity and natural gas prices, along with hourly weather data based on the year 2022, are used. The energy prices time series, as well as the relative output power of the PV modules, are shown in Fig. 5. The electricity prices are categorized into purchase $c^{buy}_{s,t,el}$ and sales prices $c^{sell}_{s,t,el}$. The sales prices are derived from spot market prices (Bundesnetzagentur | SMARD.de, 2023), while purchase prices are calculated based on the sales prices including additional factors (e.g., industrial grid fees $c^{fee}_{s,t,el}$ and taxes $c^{tax}_{s,t,el}$) amounting to around 0.06 €/kWh (Eq. (14)).

$$c^{buy}_{s,t,el} = c^{sell}_{s,t,el} + c^{tax}_{s,t,el} + c^{fee}_{s,t,el} \tag{14}$$

It is important to acknowledge that these electricity price data may not fully represent the current and future market conditions. However, due to the lack of more recent and comprehensive datasets available at the time of conducting this research, the 2022 data were utilized as the best available option. Given the primary focus on methodological application in this study, it is presumed that these data offer valuable insights into the dynamics of electricity pricing and its implications for energy system optimization, notwithstanding potential limitations. Additionally, a selling price for biomethane is assumed to be constant throughout the year. As a reference, the natural gas price for non-household customers for the year 2022 in Germany is assumed (Eurostat, the Statistical Office of the European Union, 2023). Since the biogas production happens on-site anyway and is outside the system boundary, it is available at no costs but in limited quantities.

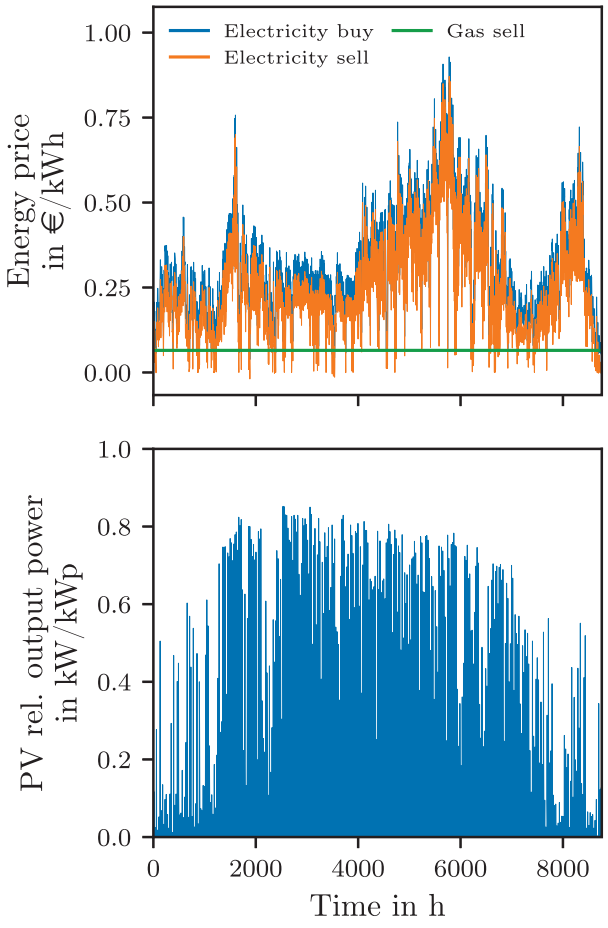

Fig. 5. Hourly reference profile of electricity and gas prices as well as the relative PV output power.

Weather data of the site in Lübeck, Germany (Pfenninger and Staffell, 2016), are converted to a relative output power of the PV modules.

Future development. For a future outlook, a low and high-value development path is assigned to each time series parameter. Utilizing these paths, the associated reference profiles are scaled accordingly. Specifically, the energy demand paths are crafted based on assumptions and tailored to align with the investment stage scheme implemented in Section 3.1.4. Fig. 6 illustrates these various paths. A more detailed explanation for each development path can be found in Appendix A.2.1. The technical and economic parameters of all components are listed in Tables A.1–A.3.

3.1.3. Scenario definition

Building upon the preceding explanations, 6 scenarios are formulated (Table 1), differing solely in the assigned development paths of the corresponding input parameters. These 6 scenarios are, in turn, grouped into 3 scenarios for each hydrogen demand path with the low and high-value assumption, corresponding to a low hydrogen demand ('LH_2', not to be confused with liquid hydrogen) and a high hydrogen demand ('HH_2'), respectively. Among these 3 scenarios, a base scenario is defined. The base scenario is designed to represent the status quo or the continuation of current trends. Consistent with the outlined trajectories (Fig. 6 and Appendix A.2.1), it assumes that the annual increase in electricity demand observed in recent years will persist into the future (high-value path). Simultaneously, it is assumed that the structure of the waste treatment plant will remain unchanged, leading to stable heat demand and biogas availability. For electricity and gas prices, a low-value path is adopted, as it more accurately reflects the price level typical of industrial operations, thereby offering a more plausible base development for this case study.

Building upon this base scenario, a 'worst-case' scenario is defined by choosing each parameter in such a way that it should be unfavorable regarding the hydrogen supply. This scenario includes high electricity prices and high electricity demand, which results in a reduction of locally produced electricity available for hydrogen production. Consequently, any shortfall must be sourced from the grid at a higher cost. Additionally, a low gas price is assumed, making the potential utilization of hydrogen for biomethane production and sale less economically attractive.

Finally, a 'best-case' scenario is defined favoring hydrogen supply. This scenario assumes low external electricity demand and low electricity costs, allowing for more locally produced electricity to be available for hydrogen production. If necessary, any additional electricity can be obtained from the grid at a lower cost. Furthermore, high gas (selling) prices and increased biogas availability are anticipated, making hydrogen production for biomethane generation more economically attractive. This, in turn, could stimulate the expansion of the hydrogen value chain.

Table 1
Considered scenarios within this work. For each input parameter, either the low-value path (L) or high-value path (H) was assigned inline with Fig. 6. (H_2: Hydrogen demand, E: Electricity (demand), BG: Biogas, H: Heat, G: Gas.)

Name	H_2	E	BG	H	E-price	G-price
LH_2 base	L	H	L	L	L	L
LH_2 worst-case	L	H	L	L	H	L
LH_2 best-case	L	L	H	H	L	H
HH_2 base	H	H	L	L	L	L
HH_2 worst-case	H	H	L	L	H	L
HH_2 best-case	H	L	H	H	L	H

Table 2
Implementation parameters.

Parameter	Value
$\|S\|$	5
n_s^y	5
n_{td}	5 per stage; incremented by 4
n_{seg}	24
α	10^{-5} kW
c^{slack}	10 000 €/kWh
i	6%

3.1.4. Implementation

In applying the method presented, the time horizon assessed here is divided into five investment stages S, each with a length n_s^y of 5 a. Within the upper bound branch, for the time series aggregation, the tool TSAM (Hoffmann et al., 2022) and the implemented hierarchical clustering method (Nahmmacher et al., 2016; Ward, 1963) are employed. The time series aggregation starts with 5 typical days n_{td} and 24 segments per year n_{seg}. In each further iteration, the number of typical days is increased by 4. To reduce the computational effort, it is assumed that, within each investment stage ($\forall s \in S$) the annual input data (e.g., energy demands, energy prices) remains unchanged. Thus, the input data for the initial year of each investment stage remains applicable throughout the entire stage and, therefore, only one representative operational optimization problem needs to be solved for each investment stage, resulting in overall $|S|$ operational optimization problems. To detect infeasible time steps, a value of 10^{-5} kW is chosen for threshold α. This threshold is intended to accommodate the solver tolerances, which typically fall within the range of 10^{-5} to 10^{-8}. As economic parameters, slack costs c^{slack} of 10 000 €/kWh are chosen and a discount rate i of 6% is assumed (Table 2).

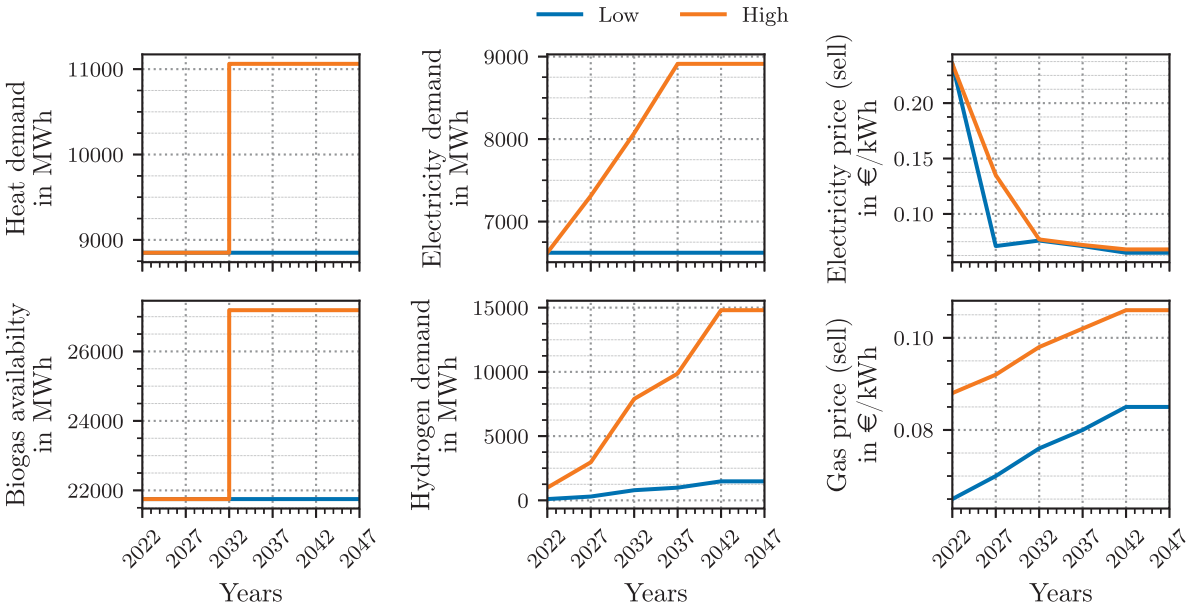

Fig. 6. Development paths of the considered input parameters. Each parameter is assigned a low and high-value path.

The energy system is modeled using the Python-based optimization framework Pyomo (Bynum et al., 2021; Hart et al., 2011). Each of the resulting multi-stage optimization problems, corresponding to the respective step within the lower and upper bound branches, is solved using the commercial solver Gurobi 10.0.0 (Gurobi Optimization, 2023). A relative optimality gap of 2% is established for each of the optimization problems in Step 2 and Step 3. Additional solver settings can be found in Table A.4. Depending on the specific case study and the resulting class of optimization problem (e.g., LP, MILP), an appropriate solver or custom solution algorithm can be selected by the user. In this study, each (sub-)optimization problem resulted in an MILP formulation, for which the widely adopted solver Gurobi is chosen. However, other solvers, such as CPLEX, are also suitable for solving these types of problems. The calculations are performed on an Intel® Core™ i7-8700K at 3.70 GHz with 12 threads and 32 GB RAM. Due to memory constraints, the total time limit for each scenario is set to 24 h before running out of memory within the lower bound branch. To prevent an iteration from being prematurely terminated and the partial results being lost, the time limit is only assessed at the beginning of each new iteration (Eq. (13)). If the limit has been exceeded, no further iterations are initiated, and the solution process for the corresponding scenario concludes. Otherwise, a new iteration begins. While this approach may result in the total computation time for a scenario exceeding the predefined time limit, the computational times in this study were found to be evenly distributed (see Fig. 7), making the results comparable across different scenarios and no further adaption necessary.

3.2. Results and discussion

In the following sections, the results obtained from applying the presented methodology to the defined case study are presented and discussed. The presentation is structured around two main parts. Firstly, the methodological performance is evaluated based on the computation time and the objective values determined. Subsequently, the results of the case study are assessed concerning the optimal system configuration. This evaluation is exemplified for a selected scenario, illustrating the type of insights attainable by the application of the presented methodology.

3.2.1. Performance evaluation

The results regarding methodological performance are presented below. Two reference comparisons are conducted to assess the quality of the methodology presented.

Firstly, a comparison is made with a commercial state-of-the-art solver in terms of computation time and solution quality. This comparison aims to quantify the computational efficiency gains achieved by applying the methodology.

Secondly, a comparison is made with a standard methodology used for solving dynamic investment or multi-stage optimization problems, which typically relies on aggregation (Pecenak et al., 2019; Mavromatidis and Petkov, 2021; Lopion et al., 2018). This comparison evaluates the improvements in solution quality and informational value provided by the proposed methodology compared to the standard approach.

For classification purposes, it is worth noting that the original optimization model contains 3 206 691 variables (937 575 binaries) and 18 469 715 nonzero elements, and is reduced to 20 000 variables (3000 binaries) and 208 405 nonzero elements within the design optimization step, respectively, 254 045 variables (105 120 binaries) and 946 088 nonzero elements during one operational optimization in the first iteration.

Comparison with state-of-the-art solver. The comparison with the state-of-the-art solver is mainly based on the computation time and the solutions found. The computation time, depicted in Fig. 7, is illustrated by the temporal progression of the upper bound (UB), lower bound (LB), and the resulting optimality gap ϵ for each 'LH_2' scenario (left) and each 'HH_2' scenario (right) (for scenario definition refer to Table 1). While the figure is designed to emphasize the overall trend rather than delve into each scenario individually, subsequent analysis will primarily focus on the 'LH_2 best-case' scenario.

The proposed method finds the first feasible solution of the original problem in approximately 3500 s. In comparison, the commercial solver Gurobi failed to find a feasible solution of the original problem within two weeks. By applying the methodology outlined above, the time needed to find a feasible solution can be reduced from more than two weeks to less than one hour (i.e., reduction of calculation by more than 99%).

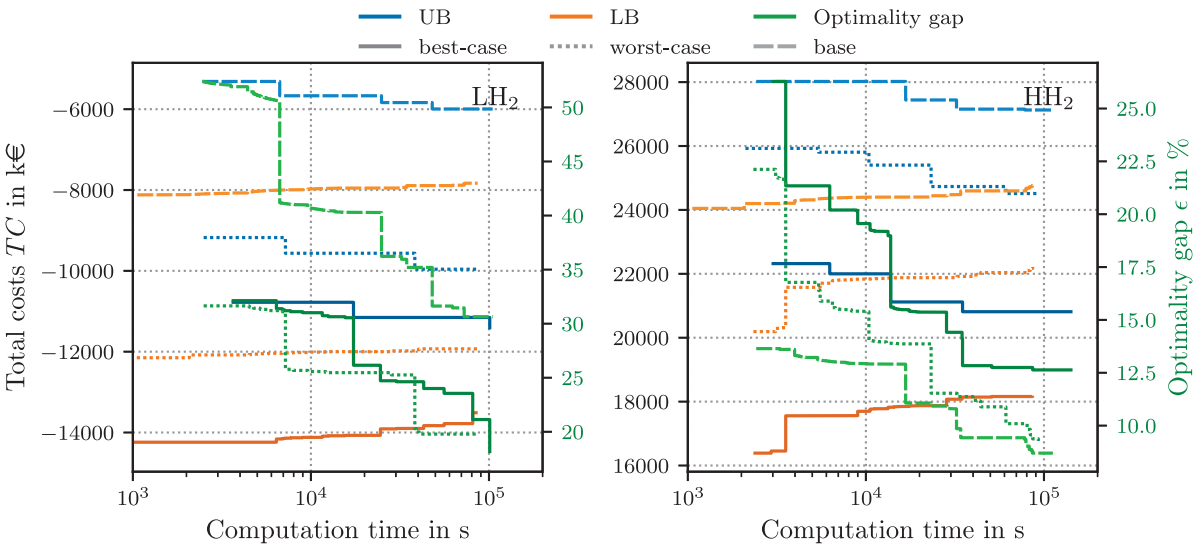

Fig. 7. Visualization of the computation time based on the progression of the upper bound (UB), lower bound (LB) and the resulting optimality gap ϵ, corresponding to the 'LH_2' and 'HH_2' scenarios.

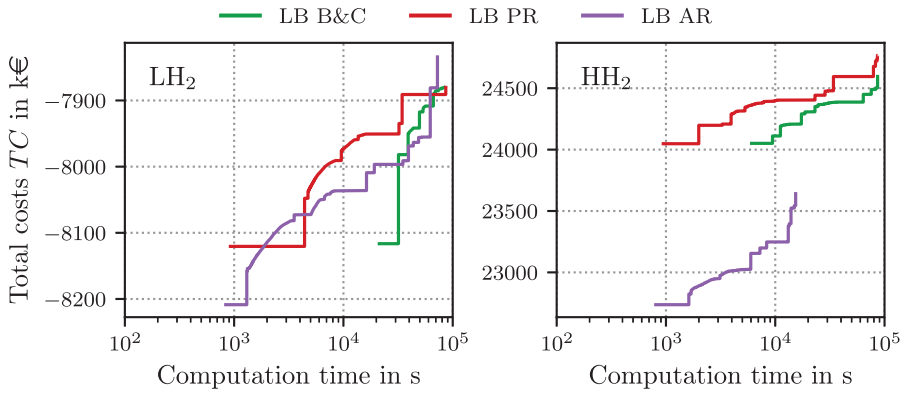

Fig. 8. Course of the computation time shown as the time progression of the three lower bound (LB) branches for the 'LH_2 base' scenario (left) and the 'HH_2 base' scenario (right) (B&C: Branch-and-Cut, PR: Pure Relaxation, AR: Aggregation & Relaxation).

A first lower bound is obtained after about 810 s. This results in an initial optimality gap of around 32%. By iteratively improving the upper bound and lower bound, the optimality gap decreases to 18% after around 24 h.

Across all 'LH_2' scenarios, the optimality gap ranges from 18% to 30% after around 24 h. In contrast, the 'HH_2' scenarios generally exhibit smaller optimality gaps, averaging around 9% to 13%. Given that the examined scenarios vary solely in input data, the time needed to achieve a competitive optimality gap is significantly influenced by the input data, among other factors. It should be noted that each of the optimization calculations performed was terminated due to the set time limit and not due to reaching a desired optimality gap. The variance in total computation time across scenarios stems from the fact that each iteration is fully completed before the time limit is checked (as detailed in Section 3.1.4). The time limit was primarily set due to memory constraints. Utilizing a different computer with greater memory capacity or relaxing the time limit to allow for longer computation times could potentially lead to further reductions in the optimality gap. However, analysis of the computational progress towards the end of each scenario indicates that only the 'LH_2 best-case' scenario showed improvement during the last iteration. Thus, the generally longer allowed computation time in the 'HH_2' scenarios is not responsible for the narrower optimality gaps observed.

The calculation of the lower bound is based on three parallel branches (see Section 2.2.2). The progression of these respective branches over time is shown in Fig. 8 for both 'base' scenarios.

It can be observed that the two relaxed branches (Pure Relaxation (PR) and Aggregation & Relaxation (AR)) produce a first lower bound after around 1000 s in both scenarios. The Branch-and-Cut (B&C) branch follows later, after approximately 6000 s for the 'HH_2' scenario and 11 000 s for the 'LH_2' scenario.

All three branches improve over time, with the AR branch ultimately showing the best lower bound after 24 h in the 'LH_2 base' scenario, while the PR branch provides the best lower bound in the 'HH_2 base' scenario.

Based on this methodology, assuming optimality convergence, the AR branch is expected to produce the fastest but also the weakest lower bound, as it contains the widest relaxation. This expectation regarding the computation time is confirmed for both scenarios, as the AR branch is the only optimization problem which is solved to optimality (HH_2: 11 000 s, LH_2: 72 000 s). The expectation regarding the weakest lower bound is at least confirmed for the 'HH_2 base' scenario. Although the PR is not solved to optimality, it provides a tighter lower bound after 24 h. In the 'LH_2' scenario, this situation differs, likely due to insufficient convergence of the PR branch, resulting in the AR branch yielding a tighter lower bound after approximately one day.

Table 3
Optimization results for the 'LH_2 base' scenario for different iterations, divided into aggregated time steps for the entire observation period, computation time per iteration, objective values after steps 2 and 3 and their resulting gap.

	Iteration 1	Iteration 2	Iteration 3[a]	Iteration 4	Iteration 5
Aggregated time steps	600	1080	1 560	2 040	2 520
Computation time in s	2282	4222	18 231	23 089	56 843
Obj. value (Step 2) in k€	−8647[a]	−8090	−7 799	−7 524	−5 047
Obj. value (Step 3) in k€	−5313	−5667	−5 836[a]	infeas.	−5 584
Gap in %	−63	−43	−34	−28	10

[a] The best solution found within iteration 3.

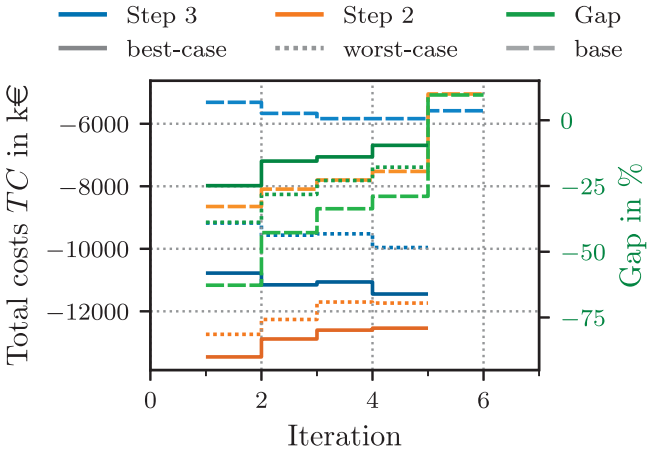

Fig. 9. Comparisons of the objective values after the aggregated design optimization (Step 2) and the year-wise operational optimization (Step 3) and the resulting gap in each iteration (refer to Fig. 2), corresponding to the 'LH_2' scenarios.

The reduced computation time of the AR branch regarding the 'HH_2' scenario suggests that the 'HH_2' scenarios are easier to solve than the 'LH_2' scenarios. It appears that the easier the optimization problem is to solve, the faster the PR branch converges towards optimality, allowing it to realize its potential of providing a tighter lower bound compared to the AR branch. Ultimately, which branch delivers a better lower bound for the user is a highly context-specific outcome, depending on the permitted computation time and the structure of the optimization problem. Therefore, a definitive conclusion cannot be drawn. Instead, it is advisable to implement all branches, leveraging the strengths of each.

Comparison with standard optimization approach. To underscore the superiority of the upper bound branch over existing methods relying solely on aggregated optimizations, Fig. 9 illustrates the objective values following the aggregated design optimization (Step 2) and the year-wise operational optimization (Step 3), along with the resulting gap for the 'LH_2' scenarios in each iteration (refer to Fig. 2 for context). In this case, the individual execution of Step 2 represents the application of a standard methodology for solving multi-stage optimization problems. While the objective values after Step 3 remain relatively stable over time, those after Step 2 exhibit substantial fluctuations. Consequently, the gap between the objective values of Step 2 and Step 3 varies widely, ranging from −63% to 10%. Notably, this pronounced fluctuation is observable even within a single scenario (Table 3), confirming the expectation that the aggregation step introduces significant inaccuracies regarding the objective value, rendering the result of the aggregated design optimization lacking reliable significance on its own.

The fluctuation's magnitude prevents making a general statement about the consistent over- or underestimation of the objective value by the aggregated design optimization. However, it is evident that, in the majority of the calculations, the objective value tends to be underestimated.

Additionally, both Table 3 and Fig. 9 illustrate that the computation time rises with an increasing number of aggregated time steps, without guaranteeing the discovery of a superior solution. Table 3 further highlights that the best solution derived from the year-wise optimization (Step 3) is attained by iteration 3 ('LH_2 base' scenario). Conversely, if based on the aggregated optimization (Step 2), this best solution would be achieved as early as iteration 1. Consequently, the same energy system configuration is not only evaluated quantitatively differently in terms of the resulting costs (objective value), but also qualitatively different energy system configurations are identified as the potentially best solution (best iteration). Compared to the proposed method, relying solely on aggregated optimization methods within multi-stage optimization problems can therefore yield suboptimal solutions that not only differ quantitatively but also qualitatively from the presumed optimal solution.

Discussion. In summary, this method significantly reduces the computing time required to find the initial solution compared to a state-of-the-art solver. However, for the final or optimal solution, it should be noted that after one day of computation, an optimality gap of 9% was achieved in the best case, but around 30% in the worst case. Importantly, without a specially adapted approach, no solution would be found at all.

This observation is well-documented in the literature (Kotzur et al., 2021), where aggregation approaches are commonly used to tackle multi-stage optimization problems (Pecenak et al., 2019; Mavromatidis and Petkov, 2021; Lopion et al., 2018; Hoffmann et al., 2020). Nevertheless, the results indicate that these standard approaches may not suffice. The findings underscore the necessity of the year-by-year optimization step to achieve more optimal and reliable results concerning target values and energy system configurations, surpassing the capabilities of aggregated optimization methods. In addition, the lower bound branch allows for a quality check of the solutions obtained, which is absent in aggregated methodologies. This quality check helps to classify and assess the reliability of the solutions achieved.

By using this method, complex multi-stage optimization problems can be solved to an acceptable proximity of the optimum in an acceptable time without compromising the certainty of the result, as is the case with the aggregated optimization step. To improve the proof of optimality, the existing approaches should be further developed to calculate tighter lower bounds.

3.2.2. Optimal system design developments

Subsequent to the methodological deliberations, the results pertaining to the case study are now under scrutiny. These results are rather intended to serve as illustrative examples, showcasing the types of outcomes attainable by the methodology. Initially, an analysis is conducted across all scenarios to scrutinize the components slated for addition in each investment phase, along with their respective capacities. Following this, a detailed examination of the optimal system configuration is undertaken, with the 'LH_2 best-case' scenario serving as an exemplar.

Scenario overview. Fig. 10 gives an overview of the bandwidth of added capacity $\Delta\hat{Q}_{c,s}$ and installed capacity $\hat{Q}_{c,s}$ of selected component types in each investment stage across all scenarios. To this end, the results (i.e., the capacity additions of the respective component at the start of each investment stage as well as the total installed capacity at this

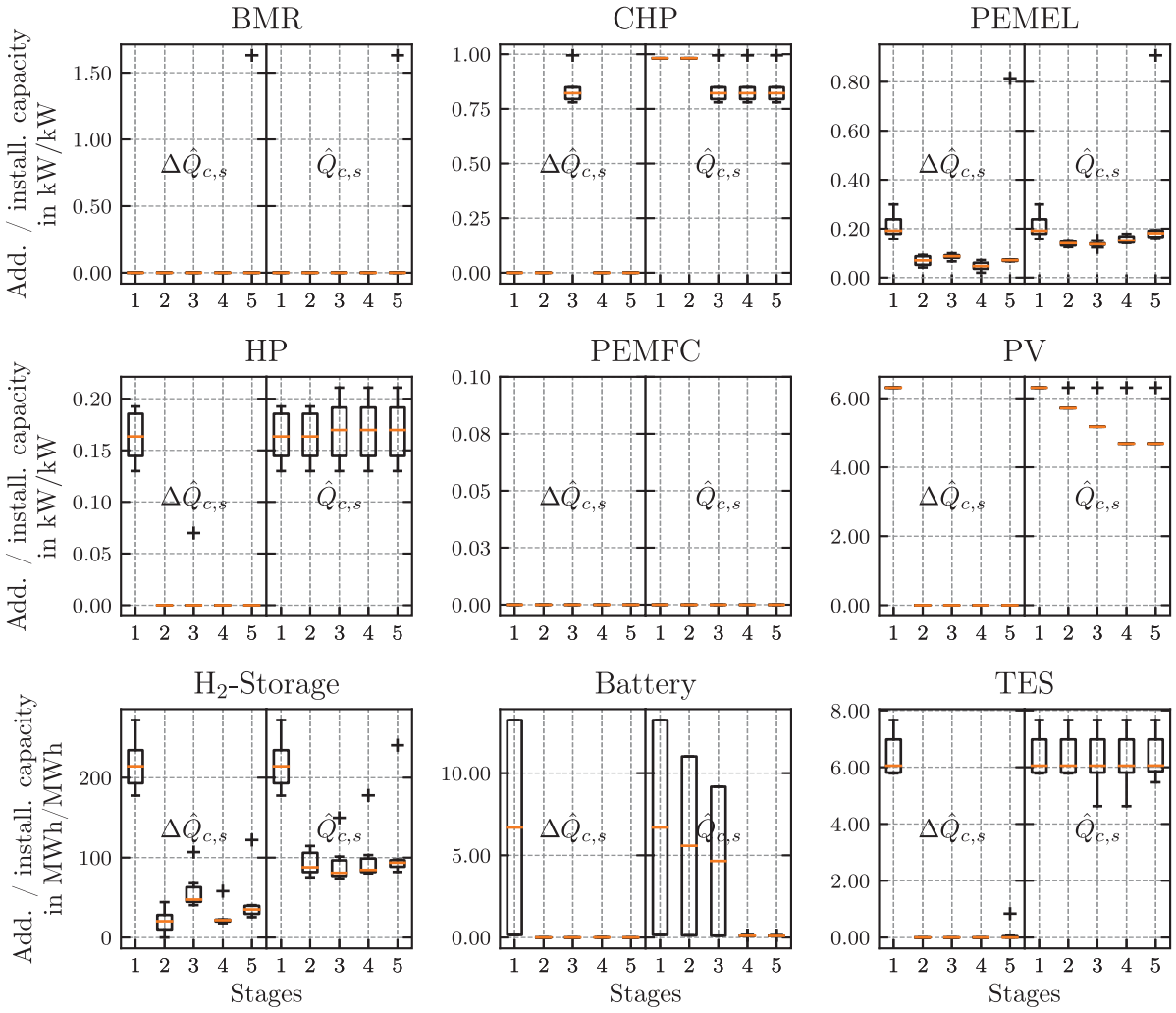

Fig. 10. Overview of added capacity $\Delta\hat{Q}_{c,s}$ (left-hand side of each subplot) and total installed capacity $\hat{Q}_{c,s}$ (right-hand side of each subplot) of selected component types in each investment stage over all scenarios. The values for the energy conversion and storage components are normalized to the maximum hourly value and the hourly average of the corresponding energy demand, respectively, to account for the progression of energy demand across different investment stages. Electricity demand: PV, Battery; Heat demand: TES, HP, CHP, PEMFC; Hydrogen demand: PEMEL, BMR, H_2-storage. Overlaying the results from each scenario provides a bandwidth (box-plot) of capacity expansion $\Delta\hat{Q}_{c,s}$ as well as the total installed capacity $\hat{Q}_{c,s}$ for each component at each investment stage. The box spans from the first quartile to the third quartile of the results data, with a line denoting the median. The whiskers reach out from the box to the outermost data point within 1.5 times the inter-quartile range from the box. (BMR: Biomethanation reactor, CHP: Combined heat and power unit, PEM: Polymer electrolyte membrane, EL: Electrolyzer, HP: Heat pump, FC: Fuel cell, PV: Photovoltaic, TES: Thermal energy storage).

point in time) of each scenario are overlaid in the form of a box plot. The energy conversion and storage components are normalized to the maximum hourly value and the hourly average of the associated energy demand, respectively. Normalization allows for the consideration of the progression of energy demands across different investment stages while ensuring comparability between scenarios (see Fig. 6). This approach helps to identify patterns related to the expansion of the respective components. The corresponding absolute values can be found in Tables A.5–A.7. It is important to note that the capacities presented below consistently refer to the primary energy output flow of each component. For instance, this corresponds to the hydrogen output power for the electrolyzer and compressor, the heat output for the heat pump, and similar measures for other components.

In all scenarios presented, a shared characteristic is the replacement of already existing combined heat and power units (CHP) by a new unit in the year 2032. This replacement results in a slight reduction of the installed capacity from 1 kW/kW to approximately 0.8 kW/kW. Nevertheless, this decrease is counteracted in every scenario by the installation of a heat pump with a capacity of approximately 0.18 kW/kW as early as 2022. Furthermore, photovoltaic (PV) systems are implemented at maximum capacity right from the outset in each scenario.

Regarding the hydrogen sub-system, electrolyzer (PEMEL) capacities are expanded in response to the rising hydrogen demand. Notably, the electrolyzers appear somewhat oversized in the initial investment stage, see a dip of the normalized installed capacity in the second stage, and exhibit continuous expansion from the third investment stage onward.

Ultimately, the installed electrolyzer capacity converges to approximately 20% of the peak hydrogen demand. Consequently, in terms of peak power, the electrolyzer is notably smaller compared to the combined capacities of CHP, heat pumps, and PV, which are sized to about 100% and 600% of the heat and electricity demand, respectively.

Furthermore, the biomethanation reactor (BMR) is built in the last investment stage in the 'LH_2 best-case' scenario. Given the low electricity and high gas prices, it appears that the investment costs for biogas methanation have decreased to the extent that biomethane production is now a more economically lucrative option than feeding excess PV electricity into the grid. In contrast, fuel cells (PEMFC) are not used at all.

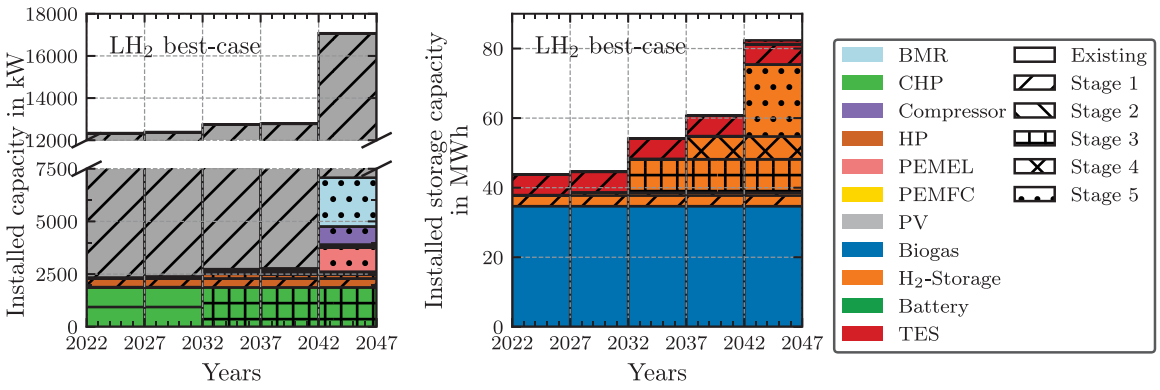

Fig. 11. Representation of the conversion and storage components system composition for each investment stage. The coloring and hatching indicate the component type and in which stage the component is built, respectively.

About the storage components, the addition of electrolyzers and compressed H_2-storage show a comparable pattern. The installed capacity of H_2-storage varies between about 100 kWh/kWh and 200 kWh/kWh in terms of average hourly hydrogen demand. Battery and thermal energy storage (TES) are also being built, mainly in the first investment stage, but to a lesser extent than H_2-storage. The installed H_2-storage capacity significantly exceeds the capacities of batteries and thermal energy storage.

The batteries and thermal energy storage are capable of covering the entire electricity and heat demand for approximately four and six hours, respectively, with a single charge. In contrast, the H_2-storage can, on average, supply the weekly hydrogen demand with one complete charge. Accordingly, long-term storage of hydrogen is not evident.

Thus, except for electrolyzers and H_2-storage, almost all components are built mainly in the first investment stage. The only exception is the CHP replacing the existing CHP without exception in investment stage 3 and outliers in biogas methanation reactor and thermal energy storage.

Scenario-specific analysis. For a more detailed analysis, the following results are presented exemplarily for the 'LH_2 best-case' scenario (for scenario definition, see Table 1). This scenario is chosen because it encompasses the broadest spectrum of achieved results. Fig. 11 presents the installed capacities of the energy conversion and energy storage components for each year. As previously detailed, it is evident that the two CHP units are replaced by a new CHP unit in the year 2032.

PV accounts for the dominant share of the installed capacity. In contrast, the installed capacities of electrolyzers and compressors are so low that they are hardly significant in the energy system context. An exception arises in the year 2042, where a biomethanation reactor unit is added for the first time. To meet the additional hydrogen demand for methanation, the inclusion of compressors and electrolyzers is appropriately scaled.

The installed capacity (in relation to the hydrogen energy content) of the compressors is lower than that of the electrolyzers. This is because the hydrogen used in methanation does not require compression, and compressors are added based solely on external hydrogen demand.

Concerning the storage components, the biogas storage remains in place, while a thermal energy storage and a H_2-storage are built at the beginning. The installed capacity of the H_2-storage increases in line with the electrolyzers at each investment stage. The proportion of hydrogen in the storage components is more significant than in the conversion components and that operating a battery, in this case, does not appear to bring any economic benefits.

Concluding, the provision of electricity and heat is primarily realized by the synergy of biogas-driven CHPs, a heat pump, and a PV system. The expansion of the hydrogen value chain primarily targets the growing demand for hydrogen to fuel waste collection vehicles. Despite the exogenous forcing of the development of a hydrogen value chain in the considered case study, hydrogen is not used for other applications (e.g., provision of electricity and heat). Its energetic utilization within a fuel cell seems less competitive compared to biogas-driven CHPs. This holds true for its application as feedstock in a biomethanation reactor as well, with one exception. Under the condition of low electricity prices and high biomethane sales prices, a case arises where the economic viability of producing biomethane from hydrogen exceeds the option of feeding surplus electricity into the grid. Thus, hydrogen is only used in situations where there is no viable alternative. Following on from the results of this section, a more detailed analysis of the costs incurred and the operating behavior can be found in Appendices A.4.2 and A.4.3, respectively.

Regarding the methodological approach of multi-stage optimization, the year 2042 marks the initial installation of a previously irrelevant technology (BMR). This underscores the importance of considering the entire transformation path rather than focusing solely on the final year in static investment optimizations. Specifically, in this case study, this insight provides the waste treatment plant operators with valuable information. By embracing multi-stage optimization, they can discern the precise year when discussions about the installation of a biomethanation reactor should commence. This temporal insight is crucial for optimizing the transformation process, revealing the dynamic relevance of technologies over time.

4. Conclusions

To comprehensively analyze future energy systems, it is imperative to consider not only the end states but also the developmental trajectory leading to them. Dynamic investment optimization models, also known as multi-stage optimization models, are essential for conducting such analyses. However, when dealing with extended time horizons and dynamic investment decisions, the resulting optimization problems often become highly complex and challenging, if not impossible, to solve within a reasonable time frame. In order to limit the computational effort, simplifications are often made which may lead to suboptimal solutions and increased uncertainty in the results.

To address this challenge, this paper introduces a rigorous optimization method tailored for multi-stage optimization problems. The method makes it possible to obtain feasible solutions for the non-simplified multi-stage optimization problem in a reasonable time. It guarantees to reach a desired optimality gap of the non-simplified optimization problem in finite time, combining state-of-the-art MILP static investment modeling techniques with multi-stage optimization

approaches without accepting any limitations related to result uncertainties.

The method is applied to a real-life multi-energy system of a waste treatment plant in Germany. For various scenarios, the possible integration of hydrogen production and usage from the year 2022 until the year 2047 is investigated. The key methodological results can be concluded as follows:

- Utilizing this method resulted in a substantial reduction in the time needed to identify the initial feasible solution, decreasing it from over two weeks to less than an hour. Across all scenarios, it was possible to demonstrate an optimality gap of around 9% after 24 h of calculation time.
- This study underscores the inadequacy of relying solely on aggregated optimization methods for multi-stage optimization problems. In this case study, total costs derived from the aggregation step deviated from actual total costs based on full time series optimization by −63% to 10%. Furthermore, the aggregated optimization results in suboptimal system configurations compared to the proposed method.
- This multi-stage optimization approach enabled the identification of periods when novel technologies were first introduced in the case study. This highlights a key distinction from static investment optimizations, as this multi-stage optimization approach unveils the dynamic relevance of technologies over time.

In the case study, the development of hydrogen production was driven by exogenous hydrogen demand. The findings regarding the case study's energy system can be encapsulated as follows:

- Despite the existing hydrogen infrastructure, the additional energetic use of hydrogen in fuel cells within the multi-energy system is not an economically competitive option. This extends to the production of biomethane in the majority of the scenarios.
- Only under specific conditions, characterized by high biomethane sales prices and low electricity prices, the study did propose the construction of a biomethanation reactor in the year 2042. Otherwise, the combination of biogas-driven combined heat and power units, heat pumps, photovoltaic systems, and corresponding storage emerged as the optimal configuration for meeting the exogenous energy demands.

In summary, the proposed method significantly advances addressing multi-stage optimization problems in multi-energy systems. The reduction in computing time enables the consideration of more complex energy systems, while the obtained results exhibit greater robustness and solutions closer to the optimum compared to prior approaches. The method facilitates a thorough analysis of the timing and types of investment decisions and the overall operation of the energy system, providing decision-makers with comprehensive and reliable information for planning and implementing investment decisions in energy systems.

Future investigations should unfold on two fronts. Firstly, exploring the method's performance in other case studies can reveal additional strengths and weaknesses. Additionally, adapting this method to other multi-stage optimization approaches, such as myopic optimization, could offer a distinct perspective on long-term energy system planning. Secondly, building on insights from the investigated case study, focusing on determining tight lower bounds promises further enhancement of the method's efficacy. Future studies should devise an approach to generate tight lower bounds within a reasonable time frame.

CRediT authorship contribution statement

Luka Bornemann: Writing – original draft, Visualization, Software, Methodology, Formal analysis, Data curation, Conceptualization. **Jelto Lange:** Writing – review & editing, Supervision, Conceptualization. **Martin Kaltschmitt:** Writing – review & editing, Supervision, Funding acquisition, Conceptualization.

Declaration of Generative AI and AI-assisted technologies in the writing process

During the preparation of this work the authors used ChatGPT in order to improve readability and language. After using this tool, the authors reviewed and edited the content as needed and take full responsibility for the content of the publication.

Declaration of competing interest

The authors declare that they have no known competing financial interests or personal relationships that could have appeared to influence the work reported in this paper.

Acknowledgments

This research is supported by the German Federal Ministry for Economic Affairs and Climate Action, Germany under the 'Green hydrogen for Lübeck's mobility of tomorrow - Hydrogen supply for the operation of a waste collection vehicle under a holistic use of all side streams - Subproject Modeling and Assessment' (HyHL) project with the funding code 03EI3055D. Publishing fees supported by Funding Programme Open Access Publishing of Hamburg University of Technology (TUHH), Germany.

Appendix

A.1. Mathematical formulation

Further constraints of the mathematical model formulation are listed here.

A.1.1. Operational constraints

The relationship between the input $\dot{Q}^{in}_{c,s,t,e}$ and output power $\dot{Q}^{out}_{c,s,t,e}$ of each energy system component ($\forall c \in C$) is modeled via Eq. (A.1) using the nominal efficiency $\eta^{nom}_{c,s}$. For computational time reasons, this is independent from the relative output power.

$$\dot{Q}^{in}_{c,s,t,e} = \frac{\dot{Q}^{out}_{c,s,t,e}}{\eta^{nom}_{c,s}}, \quad \forall s \in S, \forall t \in \mathcal{T}, \forall c \in C, \forall e \in \mathcal{E} \tag{A.1}$$

The output power is limited by the permissible partial load range (Eq. (A.2)). In case of the aggregated design optimization (refer to Section 2.2.1), $Q_{c,s}$ and $\delta^{out}_{c,s,t}$ are optimization variables, resulting Eq. (A.2) to contain a bi-linear term. Therefore, Eq. (A.2) is linearized by applying McCormick-Relaxations (McCormick, 1976; Scott et al., 2011) and by introducing the auxiliary variable $w^{out}_{c,s,t}$ to substitute the bi-linear term in Eq. (A.3).

$$\begin{aligned} \dot{Q}^{rel,LB}_{c} Q_{c,s} \delta^{out}_{c,s,t} \leq \dot{Q}^{out}_{c,s,t,e} \quad &\leq \dot{Q}^{rel,UB}_{c} Q_{c,s} \delta^{out}_{c,s,t} \\ \dot{Q}^{rel,LB}_{c} w^{out}_{c,s,t} \leq \dot{Q}^{out}_{c,s,t,e} \quad &\leq \dot{Q}^{rel,UB}_{c} w^{out}_{c,s,t} \end{aligned} \tag{A.2}$$

$$\begin{aligned} w^{out}_{c,s,t} &\geq \delta^{out,LB}_{c,s,t} Q_{c,s} + \delta^{out,LB}_{c,s,t} Q^{LB}_{c,s} \\ w^{out}_{c,s,t} &\geq \delta^{out,UB}_{c,s,t} Q_{c,s} + \delta^{out}_{c,s,t} Q^{UB}_{c,s} - \delta^{out,UB}_{c,s,t} Q^{UB}_{c,s} \\ w^{out}_{c,s,t} &\leq \delta^{out,UB}_{c,s,t} Q_{c,s} + \delta^{out}_{c,s,t} Q^{LB}_{c,s} - \delta^{out,UB}_{c,s,t} Q^{LB}_{c,s} \\ w^{out}_{c,s,t} &\leq \delta^{out}_{c,s,t} Q^{UB}_{c,s} + \delta^{out,LB}_{c,s,t} Q_{c,s} - \delta^{out,LB}_{c,s,t} Q^{UB}_{c,s} \\ &\forall s \in S, \forall t \in \mathcal{T}, \forall c \in C \end{aligned} \tag{A.3}$$

Storage components $\left(\forall c \in C^{stor}\right)$ have additional variables $SOC_{c,s,t}$ that represent the state of charge. To calculate the state of charge, time-coupling constraints are introduced, linking the state of charge between two adjacent time steps. The state of charge of the subsequent time step $SOC_{c,s,t+1}$ is calculated according to Eq. (A.4). It is based on the current state of charge $SOC_{c,s,t}$, the self-discharge rate η^{self}_{c} and the charge

$\dot{Q}^{in}_{c,s,t,e}$ and discharge rate $\dot{Q}^{out}_{c,s,t,e}$ including the associated efficiencies η^{charge}_{c} and $\eta^{discharge}_{c}$.

$$SOC_{c,s,t+1} = SOC_{c,s,t}\left(1-\eta^{self}_{c}\Delta t\right) + \Delta t\left(\dot{Q}^{in}_{c,s,t,e}\eta^{charge}_{c} - \dot{Q}^{out}_{c,s,t,e}\frac{1}{\eta^{discharge}_{c}}\right) \quad \forall s\in S,\forall t\in\mathcal{T},\forall c\in C^{stor} \tag{A.4}$$

Furthermore, the state of charge $SOC_{c,s,t}$ is limited by relative lower SOC^{min}_{c} and upper bound SOC^{max}_{c} in Eq. (A.5).

$$SOC^{min}_{c}Q_{c,s} \le SOC_{c,s,t} \le SOC^{max}_{c}Q_{c,s} \quad \forall s\in S,\forall t\in\mathcal{T},\forall c\in C^{stor} \tag{A.5}$$

To prevent charging and discharging at the same time, Eq. (A.2) is expanded for storage components in Eq. (A.6). Within the aggregated design optimization (refer to Section 2.2.1), Eq. (A.6) is relaxed in the same way, as shown in Eq. (A.3).

$$\begin{aligned}
\dot{Q}^{out}_{c,s,t,e} &\le \dot{Q}^{rel,UB}_{c}Q_{c,s}\delta^{out}_{c,s,t}\\
\dot{Q}^{out}_{c,s,t,e} &\le \dot{Q}^{rel,UB}_{c}w^{out}_{c,s,t}\\
\dot{Q}^{in}_{c,s,t,e} &\le \dot{Q}^{rel,UB}_{c}Q_{c,s}\left(1-\delta^{out}_{c,s,t}\right)\\
\dot{Q}^{in}_{c,s,t,e} &\le \dot{Q}^{rel,UB}_{c}\left(Q_{c,s}-w^{out}_{c,s,t}\right)\\
&\forall s\in S,\forall t\in\mathcal{T},\forall c\in C^{stor}
\end{aligned} \tag{A.6}$$

In addition, the state of charge is limited by a cycling constraint (Eq. (A.7)), which states that the state of charge at the beginning of an investment stage $SOC_{c,s,1}$ is identical to the state of charge at the end of an investment stage $SOC_{c,s,|\mathcal{T}|+1}$.

$$SOC_{c,s,1} = SOC_{c,s,|\mathcal{T}|+1}, \quad \forall s\in S,\forall c\in C^{stor} \tag{A.7}$$

As described in Section 2.2.1, the state of charge formulations introduced in Kotzur et al. (2018) are used within the aggregated design optimization to model long-term storage. The state of charge $SOC_{c,s,t}$ is substituted by inter-period $SOC^{inter}_{c,s,d}$ and intra-period state of charge $SOC^{intra}_{c,s,td,t}$. Additionally, the indices $td\in\mathcal{T}D$ and $d\in D$ are introduced, representing the aggregated typical days and day of the year of the full time series, respectively. The intra-period state of charge $SOC^{intra}_{c,s,td,t}$ reflects the state of charge within a typical day, while the inter-period state of charge $SOC^{inter}_{c,s,d}$ shows the state of charge over the typical days.

The intra-period state of charge $SOC^{intra}_{c,s,td,t}$ is calculated via Eq. (A.8), analogous to Eq. (A.4).

$$\begin{aligned}
&SOC^{intra}_{c,s,td,t+1} = SOC^{intra}_{c,s,td,t}\left(1-\eta^{self}_{c}\Delta t\right)\\
&+\Delta t\left(\dot{Q}^{in}_{c,s,td,t,e}\eta^{charge}_{c} - \dot{Q}^{out}_{c,s,td,t,e}\frac{1}{\eta^{discharge}_{c}}\right)\\
&SOC^{intra}_{c,s,td,1} = 0\\
&\forall s\in S,\forall td\in\mathcal{T}D,\forall t\in\mathcal{T}^{td}\subset\mathcal{T},\forall c\in C^{stor}
\end{aligned} \tag{A.8}$$

The intra-period state of charge is calculated for each typical day. For example, if the full time series is aggregated by four typical days for each stage, there are four different intra-period state of charges ($\mathcal{T}D=[1,4]$). In turn, the inter-period state of charge is formed for the full time series in each stage. For example, if an investment stage s consists of one year, there are 365 inter-period state of charges for each day of the year in each investment stage ($D=[1,365]$). Based on an aggregated chronology, one of the typical days can now be assigned to each of these 365 days. This results in a chronology for the entire year based on the typical days and allows to calculate the inter-period state of charge for the entire year in a super-positioned manner via Eq. (A.9).

$$\begin{aligned}
&SOC^{inter}_{c,s,d+1} = SOC^{inter}_{c,s,d}\left(1-\eta^{self}_{c}\Delta t\right)^{|\mathcal{T}^{td}|} + SOC^{intra}_{c,s,td(d),|\mathcal{T}^{td}|+1}\\
&SOC^{inter}_{c,s,d+1} = SOC^{inter}_{c,s,|D|+1}\\
&\forall s\in S,\forall d\in D,\forall c\in C^{stor}
\end{aligned} \tag{A.9}$$

Given low self-discharge rates (see Table A.3), the maximum and minimum state of charge within typical day td $SOC^{intra,max}_{c,s,td}$ and $SOC^{intra,min}_{c,s,td}$ (Eq. (A.10)) can be defined. These parameters are then used to limit the super-positioned state of charge for the entire period via Eq. (A.11). In this case, Eq. (A.11) replaces Eq. (A.5).

$$\begin{aligned}
&SOC^{intra,min}_{c,s,td} \le SOC^{intra}_{c,s,td,t} \le SOC^{intra,max}_{c,s,td}\\
&\forall s\in S,\forall td\in\mathcal{T}D,\forall t\in\mathcal{T}^{td}\subset\mathcal{T},\forall c\in C^{stor}
\end{aligned} \tag{A.10}$$

$$\begin{aligned}
&SOC^{inter}_{c,s,d} + SOC^{intra,max}_{c,s,td(d)} \le SOC^{max}_{c}Q_{c,s}\\
&SOC^{inter}_{c,s,d}\left(1-\eta^{self}_{c}\Delta t\right)^{|\mathcal{T}^{td}|} + SOC^{intra,min}_{c,s,td(d)} \ge SOC^{min}_{c}Q_{c,s}\\
&\forall s\in S,\forall d\in D,\forall c\in C^{stor}
\end{aligned} \tag{A.11}$$

For further information, the reader is referred to Kotzur et al. (2018).

A.1.2. Design constraints

The nonlinear investment costs are calculated via Eq. (A.12).

$$\begin{aligned}
I_{c,0} &= I^{ref}_{c}\left(\frac{Q_c}{Q^{ref}_{c}}\right)^{M_c}, && \forall c\in C\\
I_{c,s} &= I_{c,0}\exp\left(-\mu^{I}_{c}\,s\,n^{y}_{s}\right), && \forall s\in S,\forall c\in C
\end{aligned} \tag{A.12}$$

To further linearize the investment costs, the piecewise formulation from Sass et al. (2020) is applied in Eq. (A.13). The capacity $Q_{c,s}$ is discretized by $|\mathcal{J}|$ points in logarithmic distance within the bounds $\left[Q^{LB}_{c,s},Q^{UB}_{c,s}\right]$ yielding $Q^{LB}_{c,s,j}$ and $I^{LB}_{c,s,j}$ ($\forall j\in\mathcal{J}$) through Eq. (A.12).

$$\begin{aligned}
&I_{c,s} = \textstyle\sum_{j\in\mathcal{J}}\delta^{I}_{c,s,j}I^{LB}_{c,s,j} + \beta_{c,s,j}\left(Q_{c,s,j}-Q^{LB}_{c,s,j}\delta^{I}_{c,s,j}\right)\\
&\beta_{c,s,j} = \frac{I^{LB}_{c,s,j+1}-I^{LB}_{c,s,j}}{Q^{LB}_{c,s,j+1}-Q^{LB}_{c,s,j}}, && \forall j\in\mathcal{J}\\
&Q_{c,s} = \sum_{j\in\mathcal{J}}Q_{c,s,j}\\
&Q^{LB}_{c,s,j}\delta^{I}_{c,s,j} \le Q_{c,s} \le Q^{LB}_{c,s,j+1}\delta^{I}_{c,s,j}, && \forall j\in\mathcal{J}\\
&\sum_{j\in\mathcal{J}}\delta^{I}_{c,s,j} \le 1\\
&\forall s\in S,\forall c\in C
\end{aligned} \tag{A.13}$$

A.2. Input data

Additional explanations of the input data, which extend and complement the main text, are provided below.

A.2.1. Future development time series

For a future outlook, a low and high-value development path is assigned to each time series parameter. Utilizing these paths, the associated reference profiles are scaled accordingly. Specifically, the energy demand paths are crafted based on assumptions and tailored to align with the investment stage scheme implemented in Section 3.1.4. Fig. A.1 illustrates these various paths.

The electricity demand depends on further extension of the technical devices on-site.

- As a low-value path, no further extension and a constant electricity demand is considered.
- As a high-value path, the electricity demand of the considered waste treatment plant is assumed to increase by 2 %/a (Entsorgungsbetriebe Lübeck, 2021) until the year 2037. Beyond 2037, the annual electricity demand remains constant due to more efficient equipment and no further electricity extension.

The heat demand and the available biogas are coupled processes and dependent on the development of the waste treatment plant.

- As the low-value path, the waste treatment plant's composition remains unchanged throughout the assessment period. Consequently, both the annual heat demand and the available biogas will remain constant over time.

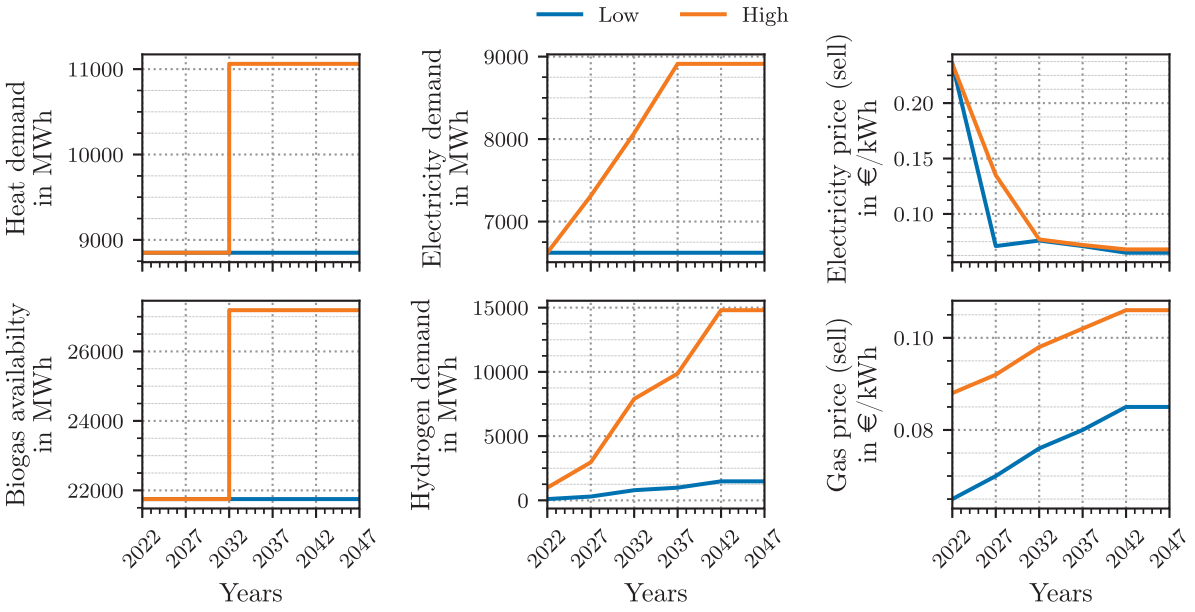

Fig. A.1. Development paths of the considered input parameters. Each parameter is assigned a low and high-value path.

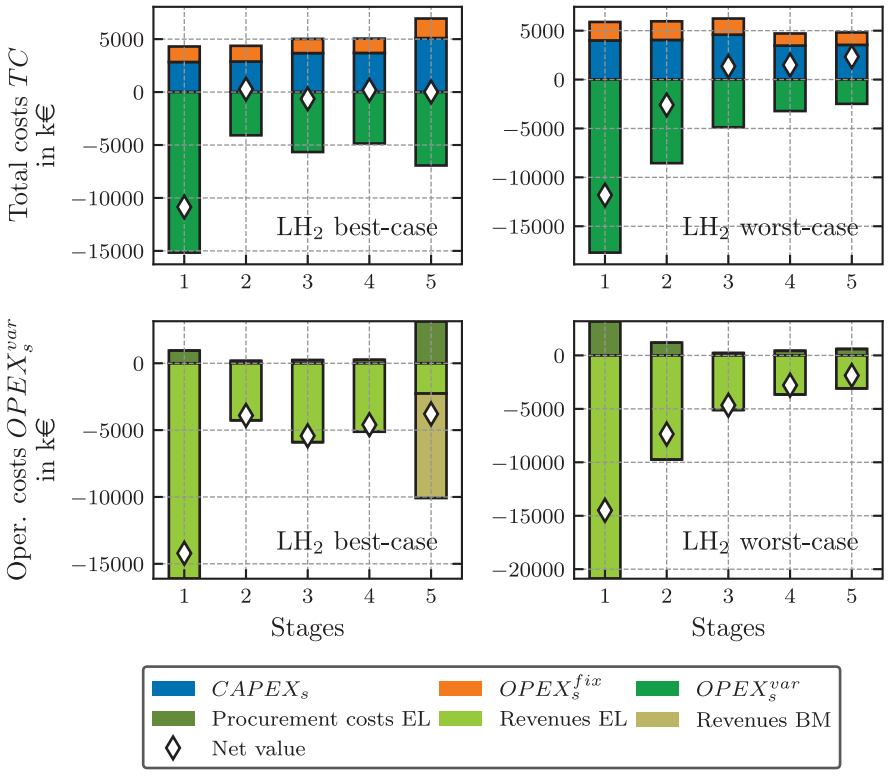

Fig. A.2. Stage-wise overview of the total costs TC and operational costs $OPEX_s^{var}$ in each scenario. (EL: Electricity; BM: Biomethane).

- As the high-value path, the addition of another digester in 2032 is assumed, resulting in a 25% increase in heat demand and biogas availability.

The fleet of 25 waste collection vehicles is to be converted to climate-neutral fuels in the coming decades.

- For the low-value case, initially one and by the year 2032, three more hydrogen vehicles are to be incorporated into this fleet, corresponding to a share of 15% (European Parliament and European Council, 2019). By 2047, a total of 15 hydrogen vehicles are be incorporated into the fleet, representing a share of 60%.
- In the high-value path, a substantial industrial expansion of hydrogen supply is assumed, amplifying it tenfold compared to the

Table A.1
Economic parameters. All monetary values are based on the year 2022. The maximum capacity to be installed is limited to 1000 MW h and 10 MW for storage and conversion components, respectively. (Q_c^{ref}: Reference capacity, I_c^{ref}: Reference investment costs, M_c: Cost-curve fitting parameter, c_c^{main}: Maintenance cost factor, μ_c^I: Long-term fitting parameter, n_c^{life}: Lifetime, deg_c^y: Yearly degradation rate).

Component	Q_c^{ref} [MW(h)]	I_c^{ref} [k€]	M_c	c_c^{main} [%/a]	μ_c^I	n_c^{life} [a]	deg_c^y [%/a]	Refs.
CHP	0.01	44.982	0.6419	10	0.005	20	2	SCCER JA S&M (2020), Voll et al. (2013) and Mavromatidis and Petkov (2021)
PV	1	1075	0.7914	1.7	0.021	30	0.25	Kost and Fraunhofer ISE (2021), Petkov and Gabrielli (2020), Sens et al. (2022) and Mavromatidis and Petkov (2021)
PEM EL	100	125e3	0.9	3.5	0.0369	15	1.5	Petkov and Gabrielli (2020), Sens et al. (2022), Skordoulias et al. (2022) and Buttler and Spliethoff (2018)
PEM FC	0.005	25	0.6889	3.8	0.0163	14	1.5	Petkov and Gabrielli (2020), Buttler and Spliethoff (2018), The Danish Energy Agency (2023a) and Clean Hydrogen Joint Undertanking (2022)
HP	1	1513	0.7744	1	0.027	25	2	The Danish Energy Agency (2023a), Mavromatidis and Petkov (2021) and Bücken et al. (2017)
Compressor	0.001	3.442	0.8335	4	0.0358	15	3.5	Sens et al. (2022), Reuß et al. (2017), U.S. Department of Energy (2022), Allen et al. (2019) and The Danish Energy Agency (2020)
Biomethanation	1	1209	0.6178	3	0.0183	20	1	Graf et al. (2014), SCCER JA S&M (2020) and The Danish Energy Agency (2023b)
Battery	1	285	0.8382	2.2	0.019	12	1.667	Petkov and Gabrielli (2020), Mavromatidis and Petkov (2021) and Sass et al. (2020)
Biogas storage	1	30.093	1	0	0	60	0	Bedoić et al. (2021)
Heat storage	23.175	502.01	0.8894	1.5	0	24	0	Petkov and Gabrielli (2020), Mavromatidis and Petkov (2021) and Sass et al. (2020)
H_2-storage	1	10	1	2.3	0.0245	23	0	Petkov and Gabrielli (2020) and The Danish Energy Agency (2020)

low-value case. This expansion opens the possibility of supplying other local companies beyond the company's vehicle fleet.

Furthermore, two trajectories for the evolution of electricity prices (Mier, 2022) are integrated. Additionally, a path for industrial and residential customers as low and high gas price cases (Kreidelmeyer et al., 2021) are defined, respectively.

A.2.2. Techno-economic parameters

The techno-economic parameters used in this work are listed in Tables A.1–A.3.

A.3. Implementation

The solver settings used, which deviate from the default configurations in Gurobi, are summarized in Table A.4 for the corresponding branches.

A.4. Further case study results

Additional case study results, which extend and complement the main text, are provided below.

A.4.1. Optimal system design developments

The absolute capacity values of the optimal system design developments of all scenarios are shown in Tables A.5–A.7.

A.4.2. Costs

Building up on the energy system development outlined in Section 3.2.2, Fig. A.2 shows each investment stage's total costs TC and operational costs $OPEX_s^{var}$ of the 'LH_2 best-case' and 'LH_2 worst-case' scenario. According to Eq. (1), the total costs include all operational and capital expenditures (OPEX and CAPEX) incurred during an investment stage to sustain the energy system being analyzed. The system configuration's low variability is reflected in the total costs as the absolute shares of investment $CAPEX_s$ and maintenance costs $OPEX_s^{fix}$ for both scenarios remain almost constant across all investment stages. The respective operating costs change significantly but always remain negative. The income from the sale of energy exceeds the costs for the procurement.

The operating costs dominate the total costs in the first investment stage ('LH_2 best-case') and the first two investment stages ('LH_2 worst-case'), resulting in an overall positive cash flow. In subsequent investment stages, operating costs rise, and thereafter, total costs per stage hover around 0 k€ ('LH_2 best-case') or 3000 k€ ('LH_2 worst-case'). In the best-case scenario, cost terms balance at the end of the observation period, while in the worst-case scenario, total costs tend to be influenced more by investment costs.

Analyzing operating costs reveals that these primarily consist of revenues from electricity feed-in, with electricity procurement costs being insignificant. A clear correlation between the electricity price trend and the electricity revenue trend is evident when compared with Fig. 6.

Table A.2
Technical parameters: Conversion units. For the compressor, the efficiency is the ratio between electrical input and hydrogen output, reflecting a multi-stage compression from 30 bar to 250 bar with intermediate cooling based on Tjarks et al. (2018) ($\dot{Q}_c^{rel}$: Relative output power, η_c^{nom}: Nominal efficiency).

Component	$\dot{Q}_c^{rel}$	η_c^{nom} [2022, 2030, 2040, 2050]	Refs.
CHP^{el}	[0.5, 1]	[0.384, 0.384, 0.384, 0.384]	Deutz (2005)
CHP^{tot}		[0.866, 0.866, 0.866, 0.866]	Deutz (2005)
PV	[0, 1]		
PEM EL^{el}	[0.1, 1]	[0.6, 0.67, 0.69, 0.71]	Sens et al. (2022) and Schalenbach et al. (2016)
PEM EL^{tot}		[0.85, 0.85, 0.85, 0.85]	Schalenbach et al. (2016) and The Danish Energy Agency (2023a)
PEM FC^{el}	[0.1, 1]	[0.5, 0.5, 0.5, 0.5]	The Danish Energy Agency (2023a)
PEM FC^{tot}		[0.84, 0.84, 0.84, 0.84]	Petkov and Gabrielli (2020)
HP	[0.2, 1]	[3, 3.28, 3.59, 3.9]	The Danish Energy Agency (2023a) and Mavromatidis and Petkov (2021)
Compressor	[0.2, 1]	[27.28, 27.28, 27.28, 27.28]	own calc.
Biomethanation	[0.2, 1]	[0.831, 0.831, 0.831, 0.831]	Graf et al. (2014)

Table A.3
Technical parameters: Storage units. The SOC bounds of the H_2-storage are based on their minimum and maximum pressure level of 20 bar and 250 bar, respectively. The data of the biogas storage is based on a real spherical gas storage with a working and cushion gas volume of 5000 N m^3 and 800 N m^3, respectively. A maximum hourly discharge rate of 30% was assumed for the biogas and H_2-storage. ($\dot{Q}_c^{rel}$: Relative output power, $SOC_c^{min/max}$: SOC bounds, $\eta_c^{(dis)charge}$: (dis)charging efficiency, η_c^{self}: self-discharge rate).

Component	$\dot{Q}_c^{rel}$	$SOC_c^{min/max}$	$\eta_c^{(dis)charge}$	η_c^{self}	Refs.
Battery	[0, 0.36]	[0, 1]	0.96	4.2e−5	Baumgärtner et al. (2020) and Kotzur et al. (2018)
Biogas storage	[0, 0.3]	[0.138, 1]	1	0	
Heat storage	[0, 1]	[0, 1]	0.95	5e−3	Sass et al. (2020)
H_2-storage	[0, 0.3]	[0.091, 1]	1	0	Reddi et al. (2018)

Table A.4
Used solver settings of the corresponding branches that deviate from the standard configurations in Gurobi.

Parameter	B&C-Branch	All other branches
mipgap	0.02	0.02
threads	0	0
Method	2	2
NodeFileStart	0.5	0.5
PreSparsify	2	2
BarHomogeneous:	0	0
MIPFocus	3	–
Heuristics	0.0001	–

In absolute terms, the initially high electricity prices do not result in elevated procurement costs but rather lead to substantial positive cash flow from the feed-in of electricity from the PV systems. The installation of PV systems amortizes within the first investment stages.

Given the abundant biogas availability at the site, the revenues consistently surpass procurement costs throughout the entire period. Even with the expansion of the biomethanation reactor in stage 5 ('LH_2 best-case'), resulting in increased procurement costs, this rise is more than compensated by the sales revenue from biomethane. In this case, the heightened procurement costs are attributed to the electricity requirements of electrolysis and the reduced availability of biogas for electricity generation in the combined heat and power (CHP) system due to methanation. Overall, the energy system generates a positive cash flow in both scenarios across the entire period.

In conclusion, despite the high availability of electricity from the combined heat and power units and the PV system, the elevated electricity prices, particularly at the beginning of the review period, establish the feed-in of surplus electricity as an unrivaled source of revenue. Nevertheless, the 'LH_2 best-case' scenario suggests that utilizing hydrogen as a feedstock has the potential to create new revenue streams. However, the realization of this potential occurs in stage 5, indicating that this assertion is more likely to hold true in the distant future. Until then, two primary conditions must be met: firstly, the investment costs for hydrogen components must decrease to compete with established technologies, and secondly, energy prices must evolve favorably to make the production of hydrogen from surplus electricity and the subsequent sale of products lucrative.

A.4.3. Operation strategy

The proposed method allows to evaluate the operation of each component for multi-stage optimizations using the full time series. In order to emphasize this special feature, further evaluations in this regard follow at this point. The input and output power of all components and the state of charge (SOC) of all storage components are exemplary displayed for investment stage 5 in the 'LH_2 best-case' scenario in Fig. A.3. All values are based on the full time series for the entire year and have been aggregated to an average weekly profile for better presentation. The input and output power are further divided into energy balances for energy carriers that are electricity, heat, hydrogen and biogas.

The electricity bus exhibits a nearly constant power demand from the electrolyzers (PEMELs) and working times correlated external peak demand. At noon, surplus electricity from PV system, most of which is fed into the grid, is evident. The CHP unit's operation is adjusted to provide electricity during periods without PV power. The CHP is complemented by the battery, charged at noon and discharged between the midday peaks. However, electricity is still drawn from the grid at night and on weekends.

The flexible operation of the CHP is also reflected in the provision of heat. It is easy to see how excess heat from the CHP is used in the evening and night hours to charge the TES and discharge it at noon. The TES contributes to stabilizing both heat supply and demand throughout the day. There are instances, especially on weekends, when the thermal energy storage (TES) and waste heat from the PEMELs fully cover the heat demand. Although a heat pump (HP) is built in every scenario, its contribution to heat provision is minimal, suggesting its construction is likely due to critical time steps.

Examining power consumption, the PEMELs operate almost continuously, with minor dips only at night when self-produced electricity is limited. Hydrogen from PEMELs is used to charge the H_2-storage outside of refueling times, which is emptied during refueling. The biomethanation reactor (BMR) is also operated almost constantly and supplied with hydrogen from the PEMELs. Despite high biogas availability, particularly on weekdays, the biogas storage facility aligns with CHP operation, loaded at noon and discharged between midday peaks.

As already explained, there are two distinctive points within a day concerning the storage components. The first is noon. Here, the battery and biogas storage are charged in line with PV and CHP while the TES is discharged. Therefore, the battery and biogas storage SOC show a

Table A.5
Installed capacities of selected component types in each investment stage for the 'base' scenarios. (BMR: Biomethanation reactor, CHP: Combined heat and power unit, PEM: Polymer electrolyte membrane, EL: Electrolyzer, HP: Heat pump, FC: Fuel cell, PV: Photovoltaic, TES: Thermal energy storage).

Component	S1		S2		S3		S4		S5	
	LH_2	HH_2	LH_2	HH_2	LH_2	HH_2	LH_2	HH_2	LH_2	HH_2
BMR	0	0	0	0	0	0	0	0	0	0
CHP	1886	1886	1886	1886	1526	1630	1526	1630	1526	1630
PEMEL	17	236	40	353	105	1010	136	1618	231	2649
Compressor	17	235	39	351	104	1005	135	1610	230	2636
HP	464	344	464	344	464	344	464	344	464	344
PEMFC	0	0	0	0	0	0	0	0	0	0
PV	10 000	10 000	10 000	10 000	10 000	10 000	10 000	10 000	10 000	10 000
H_2-Storage	2.0	21.4	3.0	27.1	9.1	66.7	11.6	90.6	15.9	138.7
Battery	118	10 000	108	9193	100	8452	108	108	100	100
TES	5.9	6.3	5.9	6.3	5.9	6.3	5.9	6.3	5.9	6.3

Table A.6
Installed capacities of selected component types in each investment stage for the 'worst-case' scenarios. (BMR: Biomethanation reactor, CHP: Combined heat and power unit, PEM: Polymer electrolyte membrane, EL: Electrolyzer, HP: Heat pump, FC: Fuel cell, PV: Photovoltaic, TES: Thermal energy storage).

Component	S1		S2		S3		S4		S5	
	LH_2	HH_2	LH_2	HH_2	LH_2	HH_2	LH_2	HH_2	LH_2	HH_2
BMR	0	0	0	0	0	0	0	0	0	0
CHP	1886	1886	1886	1886	1527	1630	1527	1630	1527	1630
PEMEL	17	282	43	421	93	1014	136	1688	230	2737
Compressor	17	419	43	419	92	1009	135	1680	229	2724
HP	454	313	454	313	454	313	454	313	454	313
PEMFC	0	0	0	0	0	0	0	0	0	0
PV	10 000	10 000	10 000	10 000	10 000	10 000	10 000	10 000	10 000	10 000
H_2-Storage	2.3	26.7	3.8	29.4	7.4	71.7	9.6	91.8	16.5	147.1
Battery	10 000	10 000	9193	9193	8452	8452	108	108	100	100
TES	5.9	7.7	5.9	7.7	5.9	7.7	5.9	7.7	5.9	7.7

Table A.7
Installed capacities of selected component types in each investment stage for the 'best-case' scenarios. (BMR: Biomethanation reactor, CHP: Combined heat and power unit, PEM: Polymer electrolyte membrane, EL: Electrolyzer, HP: Heat pump, FC: Fuel cell, PV: Photovoltaic, TES: Thermal energy storage).

Component	S1		S2		S3		S4		S5	
	LH_2	HH_2	LH_2	HH_2	LH_2	HH_2	LH_2	HH_2	LH_2	HH_2
BMR	0	0	0	0	0	0	0	0	2312	0
CHP	1886	1886	1886	1886	1872	1911	1872	1911	1872	1911
PEMEL	15	192	40	363	115	1063	133	1517	1288	2497
Compressor	15	191	40	362	114	1058	133	1509	968	2484
HP	424	363	424	363	635	363	635	363	635	363
PEMFC	0	0	0	0	0	0	0	0	0	0
PV	10 000	10 000	10 000	10 000	10 000	10 000	10 000	10 000	10 000	10 000
H_2-Storage	3.1	25.5	3.9	25.5	13.5	68.8	20.0	94.1	40.7	157.2
Battery	118	118	108	108	100	100	108	108	100	100
TES	5.8	7.3	5.8	7.3	5.8	7.3	5.8	7.3	6.9	7.3

local minimum, and the TES SOC shows a local maximum. The second point in time is refueling. Here, the H_2-storage is discharged. This also applies to the battery and biogas storage (local maximum) while the TES is charged (local minimum).

Installed capacity reflects in storage utilization. As shown in Section 3.2.2, the battery and the TES are sized for a few hours of energy demand, leading to noticeable intra-day SOC cycling between 10 % and 80 %. The H_2- and biogas storage, with larger capacity, exhibit less pronounced intra-day cycling at around Δ20 % (H_2-storage) and Δ30 % (biogas storage). Instead, an intra-weekly storage profile is also apparent. The average H_2-storage level decreases on weekdays and increases on weekends. Conversely, biogas storage sees an increasing average level over the week, sharply decreasing during the night from Sunday to Monday (no biogas production).

In conclusion, the observations outlined in Section 3.2.2 concerning the hydrogen value chain are reflected in the operational behavior. Both the PEMELs and the biomethanation reactor exhibit an almost constant supply. The aim is to achieve high capacity factors to counteract the relatively high specific investment costs. To support this, the H_2-storage largely covers peak loads. Enhancing the flexibility of PEMEL operation to reduce operating costs does not play a significant role. Additionally, it indicates that utilizing waste heat from electrolyzers can substitute heat from other supply options. However, in the considered case study, the heat demand is too substantial compared to the hydrogen demand to entirely forego other heat supply components.

Data availability

The dataset containing the results of this work is published at https://doi.org/10.5281/zenodo.13902607 under a MIT license.

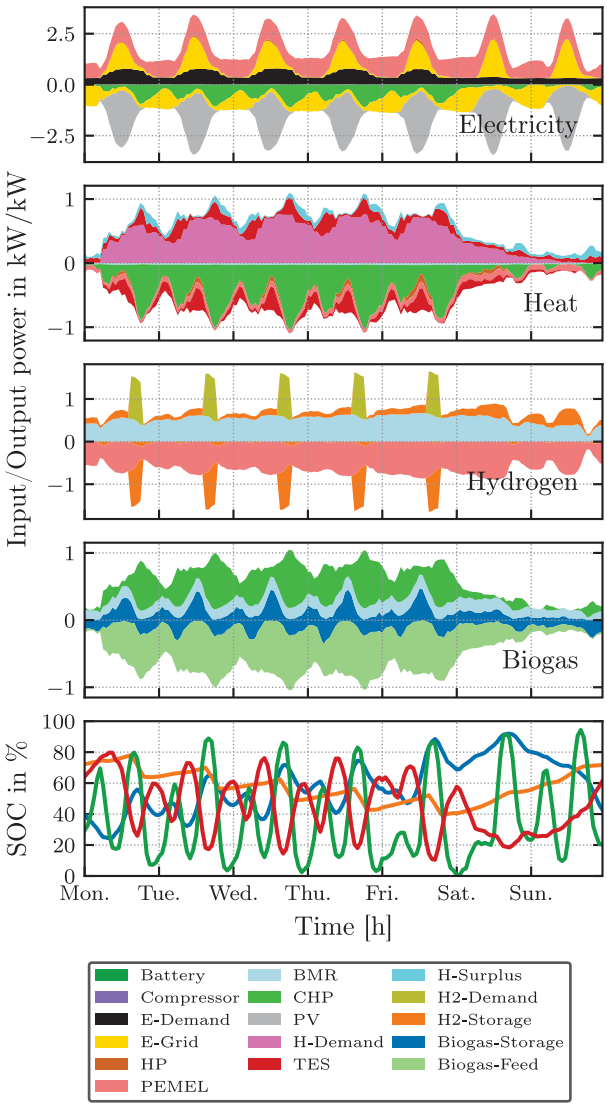

Fig. A.3. Representation of the weekly operating behavior of all components as an example of investment stage 5 in the 'LH_2 best-case' scenario. The figure is divided into the electricity, heat, hydrogen, and biogas bus energy balances and the state of charge (SOC) of the storage components. In the four upper subfigures, positive values correspond to consumers, negative values to producers. The values shown were scaled to the maximum hourly demand of the corresponding energy carrier. All values presented are based on the full time series for the entire year and have been aggregated to an average weekly profile for better presentation. (BMR: Biomethane reactor, H: Heat, CHP: Combined heat and power unit, E: Electricity; PV: Photovoltaic, HP: Heat pump, TES: Thermal energy storage, PEMEL: Polymer exchange membrane electrolyzer).

References

Allen, C.W., Holcomb, C.M., de Oliveira, M., 2019. Estimating recoverable performance degradation rates and optimizing maintenance scheduling. J. Eng. Gas Turbines Power 141 (1), http://dx.doi.org/10.1115/1.4041004.

Bahl, B., Lützow, J., Shu, D., Hollermann, D.E., Lampe, M., Hennen, M., Bardow, A., 2018. Rigorous synthesis of energy systems by decomposition via time-series aggregation. Comput. Chem. Eng. 112, 70–81. http://dx.doi.org/10.1016/j.compchemeng.2018.01.023.

Bakker, H., Dunke, F., Nickel, S., 2020. A structuring review on multi-stage optimization under uncertainty: Aligning concepts from theory and practice. Omega 96, 102080. http://dx.doi.org/10.1016/j.omega.2019.06.006.

Barthelemy, H., Weber, M., Barbier, F., 2017. Hydrogen storage: Recent improvements and industrial perspectives. Int. J. Hydrog. Energy 42 (11), 7254–7262. http://dx.doi.org/10.1016/j.ijhydene.2016.03.178.

Baumgärtner, N., Bahl, B., Hennen, M., Bardow, A., 2019a. RiSES3: Rigorous Synthesis of Energy Supply and Storage Systems via time-series relaxation and aggregation. Comput. Chem. Eng. 127, 127–139. http://dx.doi.org/10.1016/j.compchemeng.2019.02.006.

Baumgärtner, N., Shu, D., Bahl, B., Hennen, M., Hollermann, D.E., Bardow, A., 2020. DeLoop: Decomposition-based Long-term operational optimization of energy systems with time-coupling constraints. Energy 198, 117272. http://dx.doi.org/10.1016/j.energy.2020.117272.

Baumgärtner, N., Temme, F., Bahl, B., Hennen, M., Hollermann, D., Bardow, A., 2019b. RiSES4 Rigorous Synthesis of Energy Supply Systems with Seasonal Storage by relaxation and time- series aggregation to typical periods. In: Proceedings of the International Conference on Efficiency, Cost, Optimization, Simulation and Environmental Impact of Energy Systems. ECOS 2019, pp. 263–274.

Bedoić, R., Dorotić, H., Schneider, D.R., Čuček, L., Ćosić, B., Pukšec, T., Duić, N., 2021. Synergy between feedstock gate fee and power-to-gas: An energy and economic analysis of renewable methane production in a biogas plant. Renew. Energy 173, 12–23. http://dx.doi.org/10.1016/j.renene.2021.03.124.

Bohlayer, M., Bürger, A., Fleschutz, M., Braun, M., Zöttl, G., 2021. Multi-period investment pathways - Modeling approaches to design distributed energy systems under uncertainty. Appl. Energy 285, 116368. http://dx.doi.org/10.1016/j.apenergy.2020.116368, URL: https://www.sciencedirect.com/science/article/pii/S0306261920317451.

Brandon, N.P., Kurban, Z., 2017. Clean energy and the hydrogen economy. Philos. Trans. Ser. A Math. Phys. Eng. Sci. 375 (2098), http://dx.doi.org/10.1098/rsta.2016.0400.

Bücken, M., Freialdenhoven, P., Gleichmann, T., Kraft, A., 2017. Potenziale der sektorkopplung und nutzung von strom aus erneuerbaren energien im wärmebereich in Sachsen-Anhalt. URL: https://enerko.de/wp-content/uploads/2017/12/Endbericht_PtH_web.pdf.

Bundesnetzagentur | SMARD.de, 2023. Market data. URL: https://www.smard.de/en/downloadcenter/download-market-data/.

Buttler, A., Spliethoff, H., 2018. Current status of water electrolysis for energy storage, grid balancing and sector coupling via power-to-gas and power-to-liquids: A review. Renew. Sustain. Energy Rev. 82, 2440–2454. http://dx.doi.org/10.1016/j.rser.2017.09.003.

Bütün, H., Kantor, I., Maréchal, F., 2019. An optimisation approach for long-term industrial investment planning. Energies 12 (21), 4076. http://dx.doi.org/10.3390/en12214076.

Bynum, M.L., Hackebeil, G.A., Hart, W.E., Laird, C.D., Nicholson, B.L., Siirola, J.D., Watson, J.-P., Woodruff, D.L., 2021. third ed. Pyomo–Optimization Modeling in Python, vol. 67, Springer Science & Business Media.

Chertkov, M., Andersson, G., 2020. Multienergy systems. Proc. IEEE 108 (9), 1387–1391. http://dx.doi.org/10.1109/jproc.2020.3015320.

Clean Hydrogen Joint Undertanking, 2022. Strategic research and innovation agenda 2021 – 2027. 2022. URL: https://www.clean-hydrogen.europa.eu/document/download/8a35a59b-a689-4887-a25a-6607757bbd43_en.

Cuisinier, E., Bourasseau, C., Ruby, A., Lemaire, P., Penz, B., 2021. Techno–economic planning of local energy systems through optimization models: a survey of current methods. Int. J. Energy Res. 45 (4), 4888–4931. http://dx.doi.org/10.1002/er.6208.

Deng, X., Lv, T., 2020. Power system planning with increasing variable renewable energy: A review of optimization models. J. Clean. Prod. 246, 118962. http://dx.doi.org/10.1016/j.jclepro.2019.118962.

Deutz, 2005. Technische daten 50 HZ haase ET - BGA Lübeck.

Entsorgungsbetriebe Lübeck, 2020. Abfallwirtschaftszentrum Lübeck: Neue wege in der abfallwirtschaft. URL: https://www.entsorgung.luebeck.de/files/Flyer/broschuere_abfallwirtschaftszentrum.pdf.

Entsorgungsbetriebe Lübeck, 2021. Nachhaltigkeits- und umweltbericht 2020. URL: https://www.entsorgung.luebeck.de/files/Umweltbericht/umweltbericht-ebl-2020-web.pdf.

Entsorgungsbetriebe Lübeck, 2022. Entsorgungsbetriebe Lübeck (EBL): HyHL – Grüner wasserstoff aus abfall für Lübecks mobilität von morgen: Wissenschaftler der TU Hamburg untersuchen einsatzmöglichkeiten für Lübeck. URL: https://www.entsorgung.luebeck.de/ueber_uns/aktuelles/news/2022_04_28_projekt_hyhl_partner_draeger.html.

European Parliament, European Council, 2019. Directive (EU) 2019/1161 of the European Parliament and of the Council of 20 June 2019 amending Directive 2009/33/EC on the promotion of clean and energy-efficient road transport vehicles. Off. J. Eur. Union (L 188), 116–130, URL: http://data.europa.eu/eli/dir/2019/1161/oj.

European Parliament, European Council, 2021. Regulation (EU) 2021/1119 of the European Parliament and of the Council of 30 June 2021 establishing the framework for achieving climate neutrality and amending Regulations (EC) No 401/2009 and (EU) 2018/1999 ('European Climate Law'). Off. J. Eur. Union (L 243), 1–17, URL: https://eur-lex.europa.eu/legal-content/EN/TXT/?uri=CELEX:32021R1119.

Eurostat, the Statistical Office of the European Union, 2023. Gas prices for non-household consumers - bi-annual data (from 2007 onwards). URL: https://ec.europa.eu/eurostat/databrowser//product/view/NRG_PC_203.

Fu, P., Pudjianto, D., Zhang, X., Strbac, G., 2020. Integration of hydrogen into multi-energy systems optimisation. Energies 13 (7), 1606. http://dx.doi.org/10.3390/en13071606.

German Federal Government, 2021. Climate change act 2021. URL: https://www.bmuv.de/fileadmin/Daten_BMU/Download_PDF/Glaeserne_Gesetze/19._Lp/ksg_aendg/Entwurf/ksg_aendg_bf.pdf.

Government Offices of Sweden - Ministry of the Environment and Energy, 2017. The Swedish climate policy framework. URL: https://cdn.climatepolicyradar.org/navigator/SWE/2017/the-swedish-climate-policy-framework_4d29ca793f2bf5c7782ed55f5f62c434.pdf.

Graf, F., Götz, M., Wonneberger, A.-M., Köppel, W., 2014. Techno-ökonomische studie zur biologischen methanisierung bei PtG-konzepten. http://dx.doi.org/10.13140/RG.2.1.2001.9366.

Gurobi Optimization, L.L., 2023. Gurobi optimizer reference manual. URL: https://www.gurobi.com.

Hart, W.E., Watson, J.-P., Woodruff, D.L., 2011. Pyomo: modeling and solving mathematical programs in Python. Math. Program. Comput. 3 (3), 219–260.

Hoffmann, M., Kotzur, L., Stolten, D., 2022. The Pareto-optimal temporal aggregation of energy system models. Appl. Energy 315, 119029. http://dx.doi.org/10.1016/j.apenergy.2022.119029.

Hoffmann, M., Kotzur, L., Stolten, D., Robinius, M., 2020. A review on time series aggregation methods for energy system models. Energies 13 (3), 641. http://dx.doi.org/10.3390/en13030641.

Jacobson, A., Pecci, F., Sepulveda, N., Xu, Q., Jenkins, J., 2023. A computationally efficient benders decomposition for energy systems planning problems with detailed operations and time-coupling constraints. INFORMS J. Optim. http://dx.doi.org/10.1287/ijoo.2023.0005.

Kost, C., Fraunhofer ISE, 2021. Studie: Stromgestehungskosten erneuerbare Energien. 2021. URL: https://www.ise.fraunhofer.de/content/dam/ise/de/documents/publications/studies/DE2021_ISE_Studie_Stromgestehungskosten_Erneuerbare_Energien.pdf.

Kotzur, L., Markewitz, P., Robinius, M., Stolten, D., 2018. Time series aggregation for energy system design: Modeling seasonal storage. Appl. Energy 213 (4), 123–135. http://dx.doi.org/10.1016/j.apenergy.2018.01.023, URL: http://arxiv.org/pdf/1710.07593v2.

Kotzur, L., Nolting, L., Hoffmann, M., Groß, T., Smolenko, A., Priesmann, J., Büsing, H., Beer, R., Kullmann, F., Singh, B., Praktiknjo, A., Stolten, D., Robinius, M., 2021. A modeler's guide to handle complexity in energy systems optimization. Adv. Appl. Energy 4, 100063. http://dx.doi.org/10.1016/j.adapen.2021.100063.

Kreidelmeyer, S., Kemmler, A., Kirchner, A., Auf der Mauer, A., Ess, F., Piégsa, A., Spillmann, T., Straßburg, S., Wünsch, M., Ziegenhagen, I., Schlomann, B., Plötz, P., Lutz, C., Becker, L., Fritsche, U., 2021. Energiewirtschaftliche projektionen und folgeabschätzungen 2030/2050. 2021.

Li, B., Roche, R., Paire, D., Miraoui, A., 2017. Sizing of a stand-alone microgrid considering electric power, cooling/heating, hydrogen loads and hydrogen storage degradation. Appl. Energy 205, 1244–1259. http://dx.doi.org/10.1016/j.apenergy.2017.08.142.

Lopion, P., Markewitz, P., Robinius, M., Stolten, D., 2018. A review of current challenges and trends in energy systems modeling. Renew. Sustain. Energy Rev. 96, 156–166. http://dx.doi.org/10.1016/j.rser.2018.07.045.

Ma, T., Wu, J., Hao, L., Lee, W.-J., Yan, H., Li, D., 2018. The optimal structure planning and energy management strategies of smart multi energy systems. Energy 160, 122–141. http://dx.doi.org/10.1016/j.energy.2018.06.198.

Mavromatidis, G., Petkov, I., 2021. MANGO: A novel optimization model for the long-term, multi-stage planning of decentralized multi-energy systems. Appl. Energy 288, 116585. http://dx.doi.org/10.1016/j.apenergy.2021.116585.

Mazzoni, S., Ooi, S., Nastasi, B., Romagnoli, A., 2019. Energy storage technologies as techno-economic parameters for master-planning and optimal dispatch in smart multi energy systems. Appl. Energy 254, 113682. http://dx.doi.org/10.1016/j.apenergy.2019.113682.

McCormick, G.P., 1976. Computability of global solutions to factorable nonconvex solutions: Part I: Convex underestimating problems. Math. Program. (10), 147–175.

Mier, M., 2022. Erdgas- und strompreise, gewinne, laufzeitverlängerungen und das klima. 2022.

Nahmmacher, P., Schmid, E., Hirth, L., Knopf, B., 2016. Carpe diem: A novel approach to select representative days for long-term power system modeling. Energy 112, 430–442. http://dx.doi.org/10.1016/j.energy.2016.06.081.

Navas-Anguita, Z., García-Gusano, D., Dufour, J., Iribarren, D., 2020. Prospective techno-economic and environmental assessment of a national hydrogen production mix for road transport. Appl. Energy 259, 114121. http://dx.doi.org/10.1016/j.apenergy.2019.114121.

Neumaier, A., 2004. Complete search in continuous global optimization and constraint satisfaction. Acta Numer. 13, 271–369. http://dx.doi.org/10.1017/S0962492904000194, URL: https://www.cambridge.org/core/journals/acta-numerica/article/complete-search-in-continuous-global-optimization-and-constraint-satisfaction/DFCFABCCB8440B34AD3F4F1B4F3FB2A2.

Pecenak, Z.K., Stadler, M., Fahy, K., 2019. Efficient multi-year economic energy planning in microgrids. Appl. Energy 255, 113771. http://dx.doi.org/10.1016/j.apenergy.2019.113771.

Petkov, I., Gabrielli, P., 2020. Power-to-hydrogen as seasonal energy storage: an uncertainty analysis for optimal design of low-carbon multi-energy systems. Appl. Energy 274, 115197. http://dx.doi.org/10.1016/j.apenergy.2020.115197.

Pfenninger, S., Staffell, I., 2016. Long-term patterns of European PV output using 30 years of validated hourly reanalysis and satellite data. Energy 114, 1251–1265. http://dx.doi.org/10.1016/j.energy.2016.08.060.

Pot, W.D., Dewulf, A., Biesbroek, G.R., van der Vlist, M.J., Termeer, C., 2018. What makes long-term investment decisions forward looking: A framework applied to the case of Amsterdam's new sea lock. Technol. Forecast. Soc. Change 132, 174–190. http://dx.doi.org/10.1016/J.TECHFORE.2018.01.031.

Prina, M.G., Lionetti, M., Manzolini, G., Sparber, W., Moser, D., 2019. Transition pathways optimization methodology through EnergyPLAN software for long-term energy planning. Appl. Energy 235, 356–368. http://dx.doi.org/10.1016/j.apenergy.2018.10.099.

Reddi, K., Elgowainy, A., Rustagi, N., Gupta, E., 2018. Two-tier pressure consolidation operation method for hydrogen refueling station cost reduction. Int. J. Hydrog. Energy 43 (5), 2919–2929. http://dx.doi.org/10.1016/j.ijhydene.2017.12.125.

Reuß, M., Grube, T., Robinius, M., Preuster, P., Wasserscheid, P., Stolten, D., 2017. Seasonal storage and alternative carriers: A flexible hydrogen supply chain model. Appl. Energy 200, 290–302. http://dx.doi.org/10.1016/j.apenergy.2017.05.050.

Sass, S., Faulwasser, T., Hollermann, D.E., Kappatou, C.D., Sauer, D., Schütz, T., Shu, D.Y., Bardow, A., Gröll, L., Hagenmeyer, V., Müller, D., Mitsos, A., 2020. Model compendium, data, and optimization benchmarks for sector-coupled energy systems. Comput. Chem. Eng. 135, 106760. http://dx.doi.org/10.1016/j.compchemeng.2020.106760.

SCCER JA S&M, 2020. JASM - Energy conversion technologies in STEM. URL: https://data.sccer-jasm.ch/energy-conversion-technologies-stem/latest/.

Schalenbach, M., Tjarks, G., Carmo, M., Lueke, W., Mueller, M., Stolten, D., 2016. Acidic or alkaline? Towards a new perspective on the efficiency of water electrolysis. J. Electrochem. Soc. 163 (11), F3197–F3208. http://dx.doi.org/10.1149/2.0271611jes.

Scott, J.K., Stuber, M.D., Barton, P.I., 2011. Generalized McCormick relaxations. J. Global Optim. 51 (4), 569–606. http://dx.doi.org/10.1007/s10898-011-9664-7.

Sens, L., Piguel, Y., Neuling, U., Timmerberg, S., Wilbrand, K., Kaltschmitt, M., 2022. Cost minimized hydrogen from solar and wind – Production and supply in the European catchment area. Energy Convers. Manage. 265, 115742. http://dx.doi.org/10.1016/j.enconman.2022.115742.

Skordoulias, N., Koytsoumpa, E.I., Karellas, S., 2022. Techno-economic evaluation of medium scale power to hydrogen to combined heat and power generation systems. Int. J. Hydrog. Energy 47 (63), 26871–26890. http://dx.doi.org/10.1016/j.ijhydene.2022.06.057.

Stöckl, F., Schill, W.-P., Zerrahn, A., 2021. Optimal supply chains and power sector benefits of green hydrogen. Sci. Rep. 11 (1), 14191. http://dx.doi.org/10.1038/s41598-021-92511-6, URL: http://arxiv.org/pdf/2005.03464v5.

Sun, Y., Li, Z., Tian, W., Shahidehpour, M., 2016. A Lagrangian decomposition approach to energy storage transportation scheduling in power systems. IEEE Trans. Power Syst. 31 (6), 4348–4356. http://dx.doi.org/10.1109/TPWRS.2015.2511138.

Teichgraeber, H., Lindenmeyer, C.P., Baumgärtner, N., Kotzur, L., Stolten, D., Robinius, M., Bardow, A., Brandt, A.R., 2020. Extreme events in time series aggregation: A case study for optimal residential energy supply systems. Appl. Energy 275, 115223. http://dx.doi.org/10.1016/j.apenergy.2020.115223.

The Danish Energy Agency, 2020. Technology Data - Energy storage. URL: https://ens.dk/sites/ens.dk/files/Analyser/technology_data_catalogue_for_energy_storage.pdf.

The Danish Energy Agency, 2023a. Technology Data - Energy Plants for Electricity and District heating generation. URL: https://ens.dk/sites/ens.dk/files/Analyser/technology_data_catalogue_for_el_and_dh.pdf.

The Danish Energy Agency, 2023b. Technology Data - Renewable fuels. URL: https://ens.dk/sites/ens.dk/files/Analyser/technology_data_for_renewable_fuels.pdf.

Tjarks, G., Gibelhaus, A., Lanzerath, F., Müller, M., Bardow, A., Stolten, D., 2018. Energetically-optimal PEM electrolyzer pressure in power-to-gas plants. Appl. Energy 218, 192–198. http://dx.doi.org/10.1016/j.apenergy.2018.02.155.

Tong, D., Zhang, Q., Zheng, Y., Caldeira, K., Shearer, C., Hong, C., Qin, Y., Davis, S.J., 2019. Committed emissions from existing energy infrastructure jeopardize 1.5 °C climate target. Nature 572 (7769), 373–377. http://dx.doi.org/10.1038/s41586-019-1364-3.

United Nations Framework Convention on Climate Change, 2015. The Paris agreement.

U.S. Department of Energy, 2022. Hydrogen delivery scenario analysis model (HDSAM 4.0). URL: https://hdsam.es.anl.gov/index.php?content=hdsam.

Vakilifard, N., A. Bahri, P., Anda, M., Ho, G., 2019. An interactive planning model for sustainable urban water and energy supply. Appl. Energy 235, 332–345. http://dx.doi.org/10.1016/j.apenergy.2018.10.128.

Voll, P., Klaffke, C., Hennen, M., Bardow, A., 2013. Automated superstructure-based synthesis and optimization of distributed energy supply systems. Energy 50, 374–388. http://dx.doi.org/10.1016/j.energy.2012.10.045.

Wang, Y., Bornemann, L., Reinert, C., von der Assen, N., 2024. A method to bridge energy and process system optimization: Identifying the feasible operating space for a methanation process in power-to-gas energy systems. Comput. Chem. Eng. 182, 108582. http://dx.doi.org/10.1016/j.compchemeng.2023.108582.

Ward, J.H., 1963. Hierarchical grouping to optimize an objective function. J. Amer. Statist. Assoc. 58 (301), 236–244. http://dx.doi.org/10.1080/01621459.1963.10500845.

Welder, L., Ryberg, D., Kotzur, L., Grube, T., Robinius, M., Stolten, D., 2018. Spatio-temporal optimization of a future energy system for power-to-hydrogen applications in Germany. Energy 158, 1130–1149. http://dx.doi.org/10.1016/J.ENERGY.2018.05.059.

Yokoyama, R., Hasegawa, Y., Ito, K., 2002. A MILP decomposition approach to large scale optimization in structural design of energy supply systems. Energy Convers. Manage. 43 (6), 771–790. http://dx.doi.org/10.1016/S0196-8904(01)00075-9, URL: https://www.sciencedirect.com/science/article/pii/S0196890401000759.

Yokoyama, R., Takeuchi, K., Shinano, Y., Wakui, T., 2021. Effect of model reduction by time aggregation in multiobjective optimal design of energy supply systems by a hierarchical MILP method. Energy 228, 120505. http://dx.doi.org/10.1016/j.energy.2021.120505.

ZÖLLER-KIPPER GmbH, 2022. BLUEPOWER: Batterie-/wasserstoffbrennstoffzellen-antrieb. URL: https://www.zoeller-kipper.de/wp-content/uploads/2022-12-20-BLUEPOWER-DE.pdf.